PCCP

The electron-transfer intermediates of the oxygen evolution reaction (OER) as polarons by in-situ spectroscopy

Journal:	*Physical Chemistry Chemical Physics*
Manuscript ID	CP-PER-04-2021-001760.R1
Article Type:	Perspective
Date Submitted by the Author:	30-Jul-2021
Complete List of Authors:	Lyle, Hanna; University of Colorado Boulder, Materials Science Program Singh, Suryansh; University of Colorado Boulder, Materials Science Program Paolino, Michael; University of Colorado Boulder, Physics Department Vinogradov, Ilya; University of Colorado Boulder, Renewable and Sustainable Energy Institute Cuk, Tanja; University of Colorado Boulder, Chemistry Department

SCHOLARONE™
Manuscripts

ARTICLE

The electron-transfer intermediates of the oxygen evolution reaction (OER) as polarons by *in-situ* spectroscopy

Hanna Lyle[a,b,⊥], Suryansh Singh[a,b,⊥], Michael Paolino[a,c], Ilya Vinogradov[a], and Tanja Cuk[a,d,*]

Affiliations:

[a]Renewable and Sustainable Energy Institute (RASEI), University of Colorado, Boulder, Boulder, 80303

[b]Materials Science and Engineering Program, University of Colorado, Boulder, Boulder, 80303

[c]Department of Physics, University of Colorado, Boulder, Boulder, 80303

[d]Department of Chemistry, University of Colorado, Boulder, Boulder, 80303

[⊥]These authors contributed equally

[*]Corresponding Authors: tanja.cuk@colorado.edu

The conversion of diffusive forms of energy (electrical and light) into short, compact chemical bonds by catalytic reactions regularly involves moving a carrier (electron or hole) from an environment that favors delocalization to one that favors localization. While delocalization lowers the energy of the carrier through its kinetic energy, localization creates a polarization around the carrier that traps it in a potential energy minimum. The trapped carrier and its local distortion—termed a polaron in solids—can play a role as a highly reactive intermediate within energy-storing catalytic reactions but is rarely discussed as such. Here, we present this perspective of the polaron as a catalytic intermediate through recent *in-situ* and time-resolved spectroscopic investigations of photo-triggered electrochemical reactions at material surfaces. The focus is on hole-trapping at metal-oxygen bonds, denoted M-OH[*], in the context of the oxygen evolution reaction (OER) from water. The potential energy surface for the hole-polaron defines the structural distortions from the periodic lattice and the resulting "active" site of catalysis. This perspective will highlight how current and future time-resolved, multi-modal probes can use spectroscopic signatures of M-OH[*] polarons to obtain kinetic and structural information on the individual reaction steps of OER. A particular motivation is to provide the background needed for eventually relating this information to relevant catalytic descriptors by free energies. Finally, the formation of the O-O chemical bond from the consumption of M-OH[*], required to release O_2 and store energy in H_2, will be discussed as the next target for experimental investigations.

Introduction

The use of electricity to reorganize chemical bonds is at the heart of energy-storage technologies that synthesize an evolving fuel[1-2]. While electrical energy can travel extensive distances without loss, arising from the delocalization of carriers in a solid, chemical energy is stored and released from the angstrom-scale bond. The electrochemical conversion between the two is essential for flexible and renewable energy systems that release energy on demand[3]. The conversion occurs at a solid-liquid interface, which depicts the nature of the energy-storage challenge: how to convert the delocalized carriers on the solid side at a given potential into charge localized within chemical bonds on the liquid side.

The process itself requires catalysis, or the reconfiguration of chemical bonds by a series of proton and electron transfer steps, from an active site or sites that could occur either concertedly or sequentially[4-5]. In one of the most studied reactions, the oxygen evolution reaction (OER) from water ($2H_2O \rightarrow O_2 + 4H^+ + 4e^-$) that powers plant photosynthesis[6], the first electron and proton transfer step from water is often used as a descriptor of the overall catalytic activity[7]. While for molecular, homogeneous catalysts, the electron transfer is treated as arriving from a reservoir without the involvement of the solid-liquid interface[8], at a material surface the interface plays an integral role[9]. At the material surface, a bound reactive

intermediate form, denoted M-OH*,[10] catalyzes the O-O bond formation event needed to release O_2.

At the solid-liquid interface, an otherwise delocalized carrier can be trapped by a local polarization that distorts neighboring chemical bonds. The carrier is trapped within a chemical bond distance or more diffusely, across several bond-lengths. The trapped carrier and bond-distortion are together termed a polaron[11-12]. While polarons are discussed in diverse fields[13-15] and frequently associated with interfaces[16-17], the connection of the polaron to a reactive intermediate such as M-OH* has only recently been explored. Partly, this is because both a proton and electron transfer are involved in creating M-OH*; if the H^+ and e^- are explicitly in equilibrium after the transfer, then the net charge stored in M-OH* compared to $M-OH_2$ is zero. On the other hand, the binding of the oxygen to the metal site in M-OH* changes upon electron and proton transfer[18], identifying a different final electronic configuration within the metal-oxygen bond. Indeed, structural distortions associated with the electron transfer step to create M-OH* have been calculated[7, 9, 16, 19-24], albeit to different levels of theory. The oxygen within M-OH* can include terminal, lateral, and bare oxygen (without the H^+ directly bound) sites, depending on the material surface.

Moreover, recent optical and vibrational spectroscopy of OER *in-situ* on a catalytic surface has revealed bonding
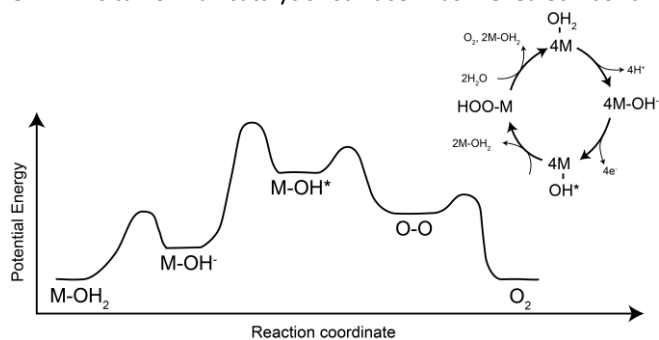
Figure 1: Potential Energy Surfaces (PES) of an OER catalytic cycle. Cycle is a multi-site mechanism for which the 4 individual electron and proton transfer steps all occur to the surface, creating 4 M-OH* prior to O-O bond formation.

configurations associated with the M-OH* intermediate[19, 25-38]. These experimental studies are carried out utilizing a full electrochemical cell. Further, they interrogate the surface during the spontaneous catalytic reaction while O_2 is evolving from a series of electron and proton transfer events (Fig. 1) driven by potential on the electrode, light excitation, or both. Importantly, the light driven reactions allow for time-resolution to isolate the kinetics associated with creating M-OH*. The time-resolved spectroscopy then targets the minima of the potential energy surfaces along the reaction coordinate of the metal-oxide bonds, as depicted in Figure 1. Most structural identifications have been associated with the first electron transfer event[19, 25, 27, 31], while others subsequent electron-transfer events[35-36], but all diagnose a reactive intermediate prior to O-O bond formation. The experiments have been conducted across a number of semiconducting, 3d transition metal oxides (TMO), which are a target for solar-to-fuel technologies[39].
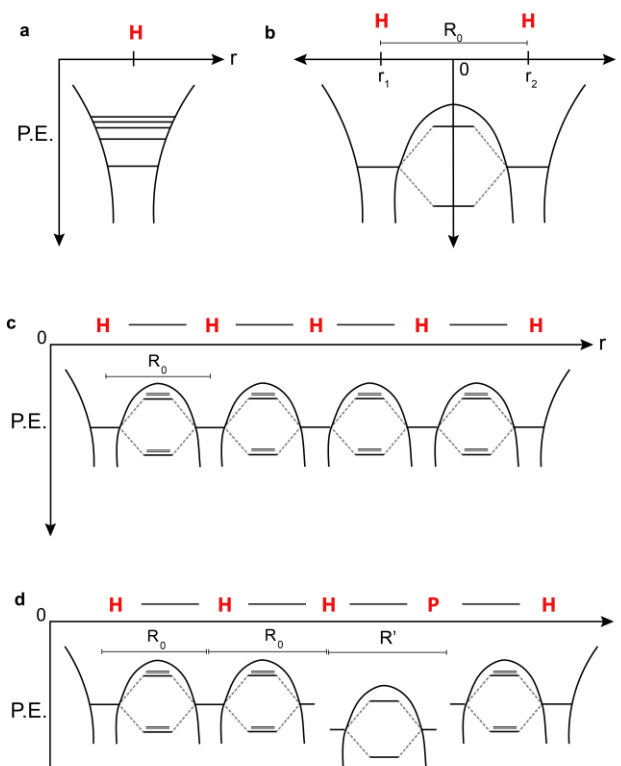
Figure 2: Potential Energy Surfaces (PES) of a H-atom (a), a H_2 molecule (b), a H-atom 1D chain (c), and a polaron (P) within the H-atom 1D chain (d).

Guided by these experimental results, this perspective highlights the M-OH* intermediate of OER as a hole-trapped polaron at the solid-liquid interface. It is divided into four sections. The first part (I. Polaron formation within an atomic chain) shortly reviews the conceptual background behind the polaron and identifies formation sites at the solid-liquid interface. The second part (II. Forming and detecting hole-polarons at 3d transition metal-oxide surfaces), focuses on the optical and vibrational signatures of hole-polarons at aqueous, 3d TMO interfaces and the associated physiochemical descriptors for their formation. The third part (III. Hole-polaron within the Oxygen Evolution Reaction (OER) mechanism), puts the hole-polaron in context of the full OER mechanism and DFT calculations of hole-polaron formation. This first half of the perspective is meant to serve as a short tutorial on structural and kinetic signatures of the polaron on aqueous 3d TMO's and situating its reaction free energy within the OER mechanism. The latter half of the perspective, the fourth part (IV. The M-OH* intermediate during *in-situ* OER by transient vibrational & optical probes) reviews the recent experimental structural and kinetic signatures of M-OH* obtained by optical and vibrational spectroscopy. We note that x-ray probes are also recently available[40] and also suggest interfacial polaron formation during OER[41-42], but are not covered here. Part IV also discusses a clear next target for the experiments, which is observing the formation of the O-O bond. Throughout, the connection of these experiments to relevant theoretical descriptors of hole-polarons and of the OER reaction itself is discussed. Concrete recommendations for future work that would enable such

critical connections between theory and experiment are listed in the concluding section (Part V: Future experimental and theoretical studies of the hole-polaron within OER).

Part I: Polaron formation within an atomic chain

We begin by summarizing some well-utilized quantum mechanical principles of the H-atom, H_2 molecule, and 1D solid chain and then situate the polaron among them[12]. The models and the associated energy levels are depicted in Fig. 2a, 2b, and 2c. The particle in a box model for how spatial scales influence the energy levels of the system is a useful one to investigate how larger length scales delocalize the electron and lower its kinetic energy at the expense of confinement. For the H-atom (Fig. 2a), as the electron becomes less spatially bound by the potential energy (PE) of the nucleus, the electronic levels rise less steeply in energy because the electron's kinetic energy lowers with decreasing confinement. On the other hand, the formation of the H-H bond in H_2 shows distinctly how the energy of the electron lowers by localizing between two H-atoms at the new minimum in the potential energy (Fig 2b). Combining the two pictures essentially gives the tight-binding approximation for orbitals in a long chain of atoms or a 1D solid (Fig. 2c). In the tight-binding model of the 1D solid, the PE minimum defines the distances between two neighboring atoms and as additional atoms are added to the chain, the orbitals hybridize across many similar bonds. The degenerate electronic levels from each atom delocalize, lowering the electron's kinetic energy akin to the particle in a box.

The polaron is the occupation of quantum mechanical levels that cannot be described fully by a homogeneous chain. A bound polaron occurs at a defect, such as an ionic center (e.g V^- or an oxygen vacancy)[11], that traps charge carriers to lattice sites within the solid. Less-bound polarons, sometimes termed "free" polarons, occur without the presence of a static defect and rather result from a fluctuation in the electronic environment that changes the local potential energy on the surface[15]; the local potential energy on the surface is referred to as a PES from here on. In either case, the resulting polaron PES arises from both deviations within the PES prior to trapping, and how that potential changes upon trapping. In effect, a unique molecular bond is formed within the solid: as a charged carrier approaches the site of the defect or fluctuation, the potential changes and creates a new minimum in the PES surface (P in Fig. 1d) unique from the other sites in the solid. While charge-carrier trapping is associated with a lower (more negative) PE minimum, its bonds could either contract or elongate compared to the chain, depending on the surrounding polarization.

This heterogeneous model of the 1D chain exhibits a concept that while inherent to quantum mechanical levels, is not explicitly present in either the molecular bond or a 1D homogeneous, tight-binding solid: the competition between gains in kinetic and potential energy[12]. As the new PE minimum is created, a local box is formed around the site, separating it from the rest of the chain such that the hybridization of the degenerate levels is simultaneously broken. Therefore, the

hole-polaron PES will have unique electronic and vibrational levels separate from those of the rest of the solid. Since these levels are no longer degenerate with their neighbors, they hybridize less, such that gains associated with the lower PE minimum are offset by increases in kinetic energy.

Therefore, the polaron sacrifices the lower kinetic energy to obtain a lower PE minimum. This is another way of posing the challenge faced by energy-storage technologies: how to store "diffuse" or kinetic forms of energy into potential energy that can be released as kinetic on demand. For a chemical reaction that utilizes intermediate bonds to a material surface to release the energy storing product, the polaron PES is essential to subsequent steps. As will be detailed in Part III, the first electron transfer step—of the formation of the polaron from the homogeneous solid—can be rate limiting for the full electro-chemical reaction.

Unlike for the generic, 1D solid with a single defect (Fig. 2d), for catalytic reactions at surfaces, many sites constitute the defects and a certain set can be more active than another. Should the termination of the solid be homogeneous, by for example an aqueous interface of adsorbed water ($M-OH_2$)[43] or hydroxyl groups ($M-OH^-$)[44-45], the surface itself constitutes repeated units in two dimensions separate from the bulk. Figure 3 depicts the cross-section of a transition metal oxide where the surface terminates with either full hydroxylation (3a) or water absorption with a hydroxyl defect (3b) at standard conditions of room temperature and atmospheric pressure. There can be empty sites at standard conditions, depending on the transition metal and the TMO structure; however, 3d transition metals prefer a molecular bonding configuration without dangling or empty bonds on the metal site. Heterogeneity within the termination—associated for example with partial dissociation of water into H_2O and OH sites—can further differentiate the "active" site for catalysis. A 50/50 partial dissociation of water stabilized by H-bonding between neighboring metal sites obtained from ab-initio molecular dynamics calculations[46-47] is shown by the planar surface of Fig. 3c.

At the solid-liquid interface, the "defect" that allows for polaron formation is the interface itself which disconnects the repeated units of the solid from the molecular configurations of
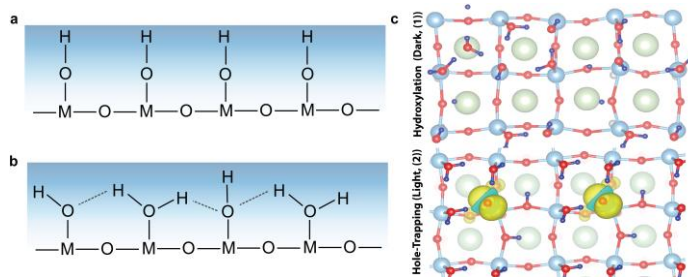
Figure 3: Surface termination of a metal oxide for a fully hydroxylated surface (a), a water adsorbed surface with a hydroxyl defect (b), and partial water dissociation (c) before and after light excitation. For (c) the planar cross-section is shown.

the liquid. The surface termination defines the shape of the polaron PES. For example, trapping a bulk hole at a dilute site of hydroxylation ($M-OH^-$) within the partially dissociated network
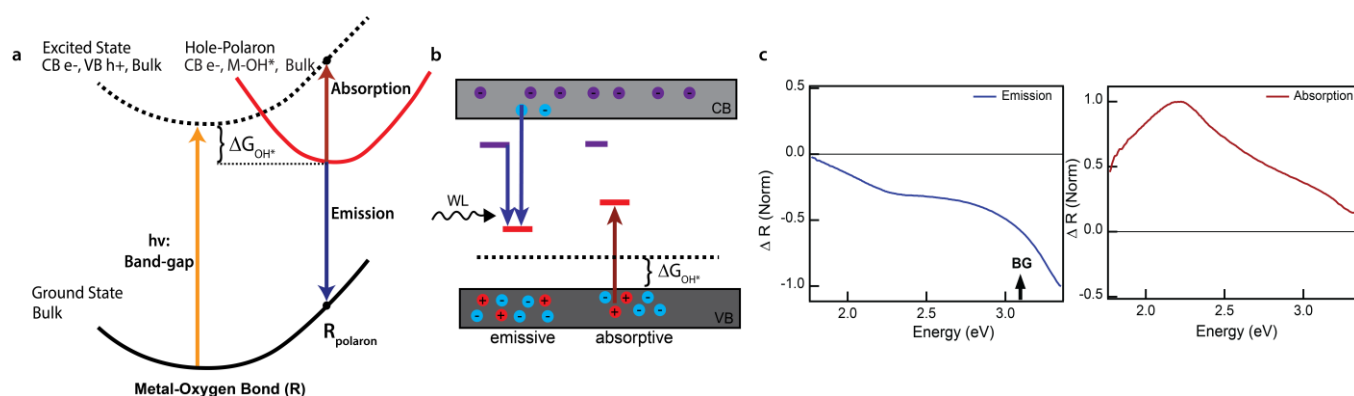
Figure 4: The absorptive and emissive transitions associated with hole polarons as depicted through the PES of the trapping event (a), a generic band diagram showing transitions involving the hole polaron energy levels (b), and the derived transitions from STO under OER conditions (c). Red, blue arrows/lines denote absorptive and emissive transitions respectively, while ΔG_{OH^*} is the free energy difference of hole-trapping.

would exhibit a lower PE minimum than at the M–OH_2 terminated sites. One of the guiding reactions for understanding surface hydroxylation across materials, especially for catalysis, is a single proton transfer reaction:

$$M\text{-}OH_2 \rightarrow M\text{-}OH^- + H^+ \quad (1)$$
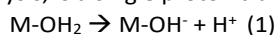
The above is discussed as the surface pK_a of the metal site, where the equilibrium constant for the de-protonation is K_a ("a" denotes acidity)[48-50]. Using the self-ionization of H_2O ($H_2O \rightarrow OH^- + H^+$), this reaction is equivalent to an exchange of hydroxyl groups (OH^-) with adsorbed water at the surface: M-OH_2 + $OH^- \rightarrow$ M-OH^- + H_2O. This representation is convenient if basic pH controls the surface hydroxylation.

Part II: Forming and detecting hole-polarons at 3d TMO surfaces

The focus of this next section is to describe the anticipated spectral and kinetic signatures of the polaron PES on a 3d transition metal oxide surface. Firstly, the electronic and vibrational levels of the polaron are described for a semiconductor TMO surface undergoing OER. The case of photo-excited holes in the valence band is considered since it most readily connects the catalytic reaction to one relevant to solar-to-fuel conversion. Secondly, the free energy differences and activation barriers associated with the transformation of a delocalized hole into an interfacial hole-polaron are discussed. The appropriate connections will be made to physio-chemical theory and descriptors, including to Marcus's electron transfer theory and to chemical equilibria.

The chemical reaction that describes a hole carrier trapped on a TMO surface site where M-OH^- is treated as a defect is:

$$M\text{-}OH^- + h^+ \rightarrow M\text{-}OH^* \rightarrow (M\text{-}O^*, H^+) \quad (2)$$

The reactant hole sits in the VB and the M-OH^- site represents an electron-dense, hole-trapping site with significant overlap with the bulk VB energy levels[16]. The actual structure of M-OH^* depends on the structure of the oxide. The * represents the meta-stable, hole trapping intermediate resulting from the electron-transfer reaction. For photo-excited VB holes that lead to O_2 evolution, this reaction is necessarily exoergic with a spontaneous ΔG_{OH^*}. Water absorbed sites (M-OH_2) could also lead to M-OH^*, but would require two hole transfers to the same site. While the hydroxylated surface traps the hole, often this is associated with H^+ release that further traps the polaron within the PES, which is then denoted by (M-O^*, H^+). The notation is deliberately generic since spectroscopically it is difficult to distinguish the location of the proton after transfer to a neighboring site.

The polarization that stabilizes the polaron can lead to significant changes in M-O bond-lengths and create new electronic states. At a semiconductor surface, these will conveniently occur within the band-gap and for hole-polarons, the quantum mechanical states will be taken from the VB states. The creation of the levels within the band-gap allows for optical transitions in the UV, visible, and near-infrared regimes to detect the polarons[11, 16, 21, 51]. Cartoons of the PES for the ground state (black line), the photo-excited state (dotted black line), and the hole-polaron (red-line) are shown in Fig. 4a, as a function of metal-oxygen bond length[11, 16, 51]. The metal-oxygen bond length could either increase or decrease depending on the polarization that traps the carrier. The emissive transition is shown as the blue arrow, where conduction band electrons reduce the polaron first at the distorted reaction coordinate ($R_{polaron}$) and then the lattice relaxes back to the minimum of the ground state surface, presumably through phonon modes. For the TMO surface, this results in recovering the M-OH^- site that is resonant with the VB levels of the bulk. The absorptive transition is shown as the red arrow, where valence band electrons instead reduce the polaron first at $R_{polaron}$ and then the lattice relaxes back to the minimum of the photo-excited surface, retaining the electron-hole excitation. The $R_{polaron}$ coordinate is the metal-oxygen bond configuration at the minimum in the hole-polaron PES. ΔG_{OH^*} is the free energy difference of the hole-trapping reaction (reaction (2)).

A simpler band diagram, more often utilized, of these transitions is shown in Fig. 4b. The red lines indicate the vertical transitions implied by the PES for both absorptive and emissive transitions from the CB and VB respectively; these are in general different and depend on the Frank-Condon overlap with the hole-polaron PES. Representative absorptive and emissive spectra during OER on a titania perovskite, $SrTiO_3$ are shown in Fig. 4c. As might be anticipated, these are fairly broad transitions involving not only the Frank-Condon overlap, but

also geometrically diverse M-OH* that could in principle diffuse [16, 21], which we return to in Part IV with the *in-situ* experiments.
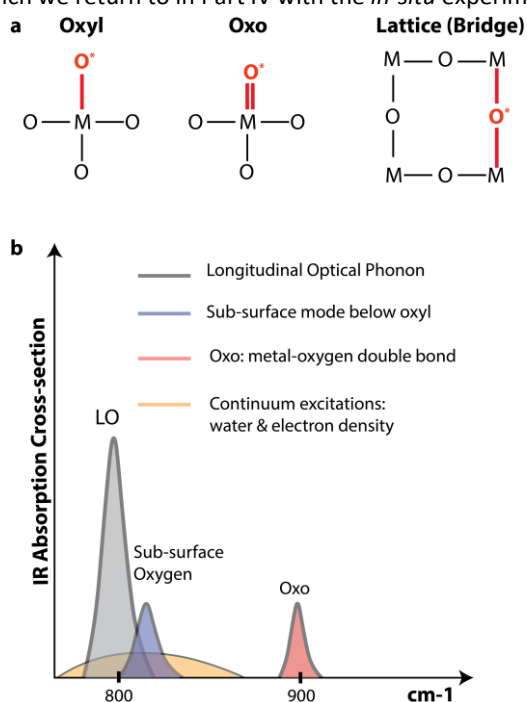

Figure 5: Vibrational transitions associated with the configurations of metal-oxide hole polarons, depicted in terms of the local bonds in a), and within an infrared spectrum (b). In (c), the oxo (pink), and oxyl (purple) configurations are depicted next to the LO phonon (gray); the yellow represents nearby continuum excitations.

Using Fermi's golden rule, the optical transition in a one-dimensional spectroscopy will be a convolution of the density of states (DOS) of the initial and final states. For the absorptive transition, the initial state includes that of the surface hole-polaron and a bulk VB electron on the hole-polaron PES, while the final state is an excited vibrational state of the photo-excited PES (dotted black line, Fig. 4a). For the emissive transition, the initial state includes that of the hole-polaron and a CB electron on the hole-polaron PES, while the final state is an excited vibrational state of the ground state PES (solid black line, Fig . 4a). The implication is that the optical spectrum, in principle, will reflect the hole-polaron DOS to a greater or lesser degree depending on the degree of delocalization of the bulk VB and CB states (*i.e.* the shape of the photo-excited and ground state PES's). Further, the time-evolution will be an interplay of CB occupation and hole-polaron populations for the emissive transitions, and VB occupation and hole-polaron populations for the absorptive transitions.

The polaron PES will also give rise to new vibrational levels, and should the polaron be localized to a couple of bond-lengths, vibrational transitions will detect new, well-defined normal modes. Depending on the polarization, one can expect either a contraction or elongation of the surface bond compared to the bulk. The creation of an "oxo" intermediate implies a double bond between the metal and the surface oxygen, e.g. M=O* (Fig. 5a). The appearance of a double bond has been observed during OER in the later transition metal (Fe, Mn, Co) oxides[27, 31, 35-36]. On the other hand, the creation of an "oxyl" intermediate

(Fig. 5a) creates a radical species (M-O$^{\bullet-}$) associated with more charge trapped on the oxygen and a bond elongation. Such a distortion is inherently difficult to detect since a new bond does not accompany it, but as will be described below, a sub-surface vibration resulting from the distorted surface bonds arises in $SrTiO_3$[25]. While the oxo occurs in the range of 900 cm^{-1}, the sub-surface mode of the oxyl occurs on the high energy side of the longitudinal optical phonon (Fig. 5c). Finally, hole-polarons could also be created at lateral sites of the oxide as depicted in Fig. 5a; these are also referred to as lattice or bridge sites of the
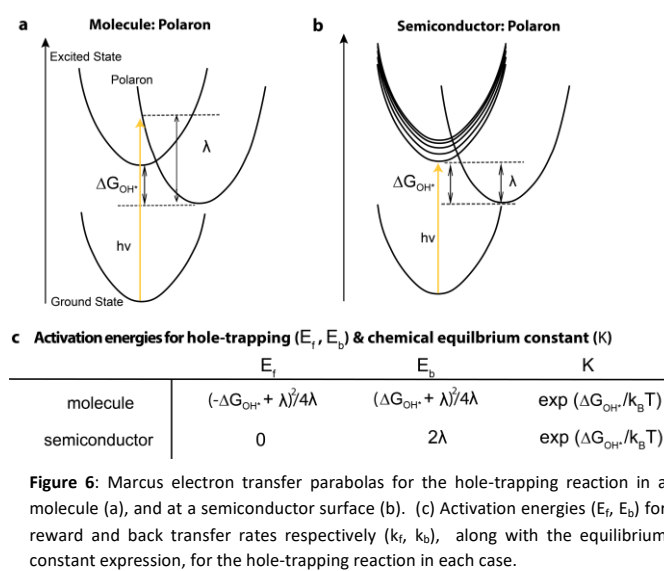
Figure 6: Marcus electron transfer parabolas for the hole-trapping reaction in a molecule (a), and at a semiconductor surface (b). (c) Activation energies (E_f, E_b) for reward and back transfer rates respectively (k_f, k_b), along with the equilibrium constant expression, for the hole-trapping reaction in each case.

oxide[19]. These have yet to be detected vibrationally, by either experiment or calculation to our knowledge.

With the above description of the essential spectral signatures of the hole-polaron, we now turn to describing the kinetic rates of forward and back electron transfer of the hole-trapping reaction. One can place these rates both within Marcus electron transfer theory and more generally, the concept of chemical equilibria. For Marcus theory, we again invoke the PES's of the ground state, the photo-excited, and the polaron as shown in Fig. 6. The forward and back electron transfer rates are derived by casting the photo-excited and the polaron PES as parabolas:

$$k_f = \nu e^{\left[-\frac{(\Delta G + \lambda)^2}{4\lambda k_B T}\right]} \& k_b = \nu e^{\left[-\frac{(-\Delta G + \lambda)^2}{4\lambda k_B T}\right]} \quad (3)$$

in which ΔG will refer to the free energy difference of the hole-trapping reaction (2), ΔG_{OH^*}. λ is the Marcus reorganizational energy[52] released to the surroundings in trapping a hole on the photo-excited PES at the distorted $R_{polaron}$ coordinate; ν is the diabatic overlap between the two excited state PES's that allows for a transition between the two surfaces. Fig. 6a shows these curves in the absence of a band description, where the hole is created at a particular site, such as M-OH$^-$ and Fig. 6b shows them in the presence of the band description, where the hole is truly delocalized. In the molecular case, the activation energy for forward hole transfer to the favored $R_{polaron}$ configuration, $(\Delta G + \lambda)^2/4\lambda$, can still be quite large due the reorganizational

energy λ. With the introduction of the band description of the solid, the electronic levels lead to an activation-less transition as elucidated by J. Cheng, J. VandeVondele, and M. Sprik[16]. In this case, ΔG released to the surroundings is equal to the reorganizational energy ($\Delta G = -\lambda$), such that the transition occurs at the "maximum" of the Marcus curve. Therefore, the forward transfer (k_f) is activation-less, while the back-transfer (k_b) has a large activation barrier (Fig. 6c). Thus, creating a delocalized carrier first in the solid allows for both efficient polaron formation and stability with respect to back-transfer. A transient, ultrafast spectroscopy could obtain the forward and backward rates directly by time-resolving the polaron population *in-situ* during the electrochemical reaction.

Since several electron-transfer and chemical steps constitute the full reaction, the back transfer rate of the polaron will be convolved with the forward transfer rate towards O-O bond formation. It would therefore be quite helpful to identify ratios of forward and backward reactions in addition to time-resolving each separately. Indeed, the ability to separate the full reaction into several reaction steps suggests that each step leads to an effective equilibrium definable by the meta-stable intermediate populations. Further, identifying such equilibrium constants would allow for kinetic events, the direct observables in the time-resolved spectroscopy, to be connected to thermodynamic free energy differences between intermediates using:

$$K = \frac{k_f}{k_b} = e^{-\frac{\Delta G}{kT}} \qquad (4)$$

Finally, in the context of dark, thermochemical events which do not involve electron transfers from the bulk of the solid, the kinetics would rather be guided by transition state theory[53], involving an activation free energy, ΔG^χ, that describes the difference between the potential energy minimum of the hole-polaron and the thermodynamic state at the top of the activation barrier to the next step (Fig. 1). Such a dark thermochemical event utilizing hole-polarons has been proposed to initiate O-O bond formation.

Part III: Hole-polaron at 3d TMO surfaces within OER mechanism

The above introduced the hole-polaron from the perspective of its quantum mechanical states and defined its spectroscopic signatures at a TMO surface. The reaction kinetics were treated in isolation of the OER cycle. In this section, we put the M-OH* hole-polaron reaction kinetics in context with the rest of the steps. As forwarded by DFT calculations of electrochemical interfaces, this is done by utilizing the ΔG of each reaction step and the "scaling" relationships between them. After describing these scaling relationships and the OER scheme, we also discuss important differences for a photo-driven reaction at a semiconductor-liquid interface. Finally, DFT and AIMD calculations for the ΔG_{OH^*} of M-OH* on $3d^0$ TiO$_2$ surfaces are summarized and situated within the OER mechanism.

The reaction steps cited for the OER mechanism are delineated in Table 1, with their free energy differences: H$_2$O/OH* (ΔG_1), OH*/O* (ΔG_2), O*/O-O (ΔG_3), and O-O/O$_2$ (ΔG_4)[10]. The value of these free energy differences is a function of the electrode potential, from which the electron transfers arise, as shown for a couple of potentials in Figure 7a. Only with enough potential (here 1.6 V vs. the reversible hydrogen electrode, RHE), does each reaction step proceed with a negative ΔG to evolve O$_2$ spontaneously. In an ideal catalyst, the active site is infinitely tunable such that when the electrode potential is set to the Nernstian potential of the reaction, 1.23 V vs. RHE, the free energy of each reaction step is zero and the addition of a very small "over-potential" would cause the cycle to proceed spontaneously.
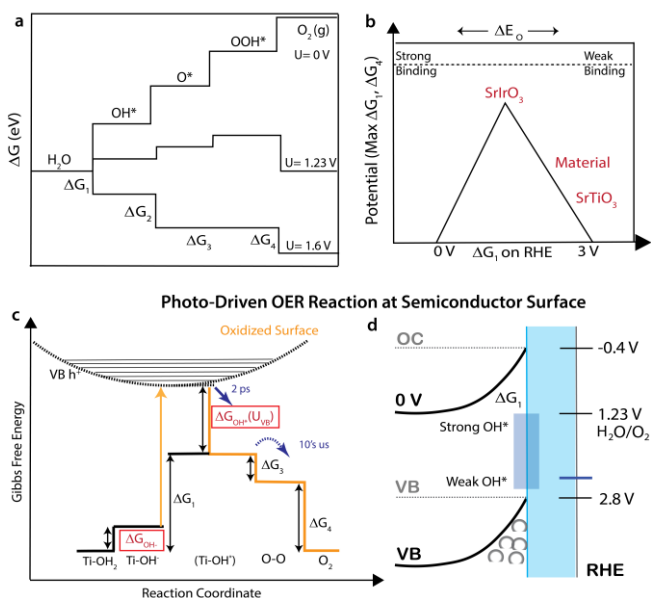
In a practical catalyst, for which the ground electronic state of a material circumscribes the nature of the active site, the reaction is simplified to the most relevant material descriptor. This is achieved by utilizing three assumptions that constrain the problem and translate free energy differences into an activity of product evolution: (1) a single site mechanism, (2) single electron and proton transfer events which happen sequentially in the OER scheme, leading to the four ΔG and (2) scaling relationships between the individual ΔG.[9, 18, 20] The two assumptions are interrelated: since a single site is not suited to evolve different chemical intermediates with the same facility, the ΔG are interdependent. The two primary scaling relationships are: $\Delta G_1(OH^*) = \Delta G_2(O^*)$ and $\Delta G_3(OOH^*) = 3.2$ eV - $\Delta G_1(OH^*)$.[9] The former is suggested to be the case by

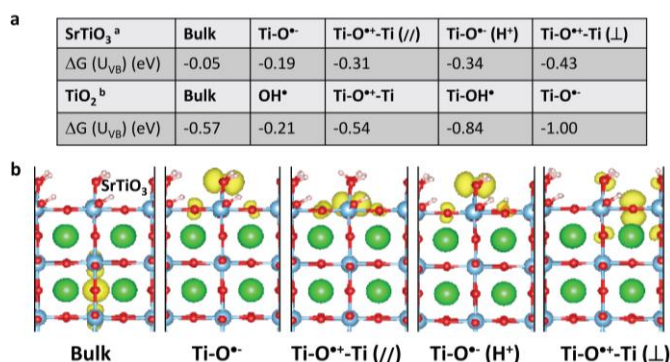| Photo-driven OER (Multi-site)		Potential-driven OER (Single-site)
$4M - OH_2 \leftrightarrow 4M - OH^- + 4H^+$	$\Delta G_0 = \Delta G_{OH^-}$	
$4M - OH^- + 4h^+ \rightarrow$ $4M - OH^* \rightarrow 4(M \overset{...}{\cdots} O^*, H^+)$	ΔG_1 $\Delta G_{OH^*}(U_{VB})$	$M - OH_2 + h^+ \rightarrow M - OH^* + H^+$
Only in single site mechanism for weak binding	ΔG_2	$M - OH^* + h^+ \rightarrow M - O^* + H^+$
$4(M \overset{...}{\cdots} O^*, H^+) \rightarrow$ $M - O - O^* - M + 2M - OH_2$	ΔG_3	$M - O^* + H_2O + h^+ \rightarrow M - O - OH^* + H^+$
$M - O - O^* - M + 2H_2O \rightarrow$ $O_2 + 2M - OH_2$	ΔG_4	$M - O - OH^* + H_2O + h^+$ $\rightarrow O_2 + H^+ + M - OH_2$

Table I: Reaction mechanism for photo-driven reaction depicted in terms of a free energy landscape in Fig. 6c for a multi-site mechanism (left). Reaction mechanism for a purely potential driven, single-site mechanism on a metal (right). In the photo-driven mechanism, the first ΔG is separated into a proton transfer (ΔG_0) and a subsequent hole-transfer from the solid (ΔG_1) to reflect the equilibrated surface in the dark prior to excitation of photo-holes. For a more facile comparison, the electron transfers are all written as reactant holes, for both the photo-driven and potential-driven mechanisms. The reactant hole is at the electrochemical potential of the electrode.

calculation for a subset of 3d TMOs. The latter arises from a single-site mechanism for which the only difference between M-OH* and M-OOH* is the O-O bond. With these scaling relations, the free energy difference for the final step of O_2 evolution becomes $\Delta G_4 = 4.92$ eV - $2\Delta G_1$ - ΔG_3, where 4.92 eV is constrained by the total reaction ΔG. Since all of the individual ΔG then scale with each other, one practical descriptor out of the four emerges to define the total activity for OER. A minimum potential needed to level the largest ΔG (U= 1.6 V in Fig. 6a) is then determined to make the reaction spontaneous. Often, $\Delta G_1(OH^*)$ or $\Delta G_2(O^*)$ is chosen as the theoretical descriptor of the OER activity[7]. First, it can be the largest one for many TMO's.[20] Second, these reaction free energies are most relatable to the change in electronic binding energy of the oxygen to the metal site after a single proton and electron transfer, or ΔE_O.[10] However, ΔE_O can be included using different elementary reactions, leading to differently reported values. Whichever method is chosen, ΔE_O should then be related to the ΔG's within the OER scheme to describe the OER activity. Because of these issues and since the experiments primarily concern the first electron and proton transfer from water, $\Delta G_1(OH^*)$ will be utilized as the primary descriptor.

"Volcano plots" are constructed as a function of ΔG_1 (OH*) which includes the change in the binding energy of oxygen in the M-OH* intermediate with respect to M-OH$_2$ within it. An example is shown in Fig. 7b. In this plot, the x-axis is ΔG_1, while the y-axis is the potential that is needed for the reaction to be spontaneous. On the left branch of the volcano for which ΔG_1 is small, ΔG_3 (O-O forming) is rate limiting, while on the right branch, ΔG_1 is large and rate limiting; these are also called the "strong-binding" side with an increasingly exothermic ΔE_O and a "weak-binding" side with an increasingly endothermic ΔE_O. A

Figure 8: (a) The free energy difference for hole-trapping to create M-OH* in TiO_2 from ref. 16 and SrTiO$_3$ from ref. 19 for various configurations, including bulk hole-polarons. (b) The hole-polaron structures for various configurations on SrTiO$_3$. The two oxyl's differ in the location of the proton. The two bridge intermediates differ in the orbital orientation and location of the proton.

similar physical reasoning for oxygen-binding as a thermodynamic descriptor of activity has been advanced in other contexts, namely the d-band theory of metals[54] and more recently, the occupation of the e_g orbital in perovskites[55]. These emphasize how the $\Delta G_1(OH^*)$ or $\Delta G_2(O^*)$ are guided by the ground state electronic (or molecular orbital) structure of the TMO.

In applying this methodology to the photo-driven reaction at a semiconducting oxide-liquid interface, as opposed to a purely potential driven reaction at a metal-liquid interface, one needs to consider two general issues. Firstly, the initial reaction step will be different since the photon excites an equilibrated semiconductor-liquid interface essentially instantaneously. Secondly, all the reaction steps occur within a fairly large electric field in the aqueous electrolyte that screens the charge in the electrode (the Helmholtz layer), which will be different for a metal than a semiconducting oxide. We address the first point here, since this leads directly to a different manifestation of the first reaction step, whereas the latter concerns primarily the environment in which the first and later steps take place (in the absence of specific adsorption). A depiction of the photo-driven reaction in terms of free energy differences between intermediate forms is shown in Fig. 7c. Prior to light excitation, the sample equilibrates with the electrolyte in the dark (solid black line), for which the relevant reaction is a simple proton transfer modulated by pH and defined by the pK$_a$ of the metal site, ΔG_{OH^-} (reaction (1) in Part I and in Table I). Upon light excitation, VB holes drive the reaction downhill. Thus, the relevant electron-transfer reaction to create the first OER intermediate, M-OH*, is equivalent to the hole-trapping (reaction (2) in Part I and in Table I). $\Delta G_{OH^*}(U_{VB})$ denotes the free energy difference between the delocalized VB hole at U_{VB}, the VB edge potential, and the trapped hole in the semiconductor.[16] Since this is a simple electron transfer not involving a proton, $\Delta G_{OH^*}(U_{VB})$ can also be related to a Marcus reorganizational energy, as delineated in Part II (Fig. 6c).

Table I shows the reaction steps for a photo-driven mechanism alongside the purely potential-driven one. The photo-driven scheme differs in two primary ways. First, it starts from an equilibration of the surface with the electrolyte defined

Figure 7: (a) Free energies of individual OER reaction steps as a function of potential on the electrode in a purely potential driven mechanism. (b) The free energy of the first electron and proton transfer step (ΔG_1) as a descriptor of total OER activity in a Volcano plot. (c) The free energies of the individual OER reaction steps when driven by photo-excitation of a semiconductor. (d) ΔG_1 plotted on the electrochemical scale along with the semiconductor band edges.

by the surface pK$_a$, which only involves a proton transfer. Introducing the pK$_a$ of a metal site through $\Delta G_0 = \Delta G_{OH^-}$ essentially separates the H$^+$ transfer from the electron transfer in the usual OER scheme that includes both in ΔG_1 ($M - OH_2 + h^+ \rightarrow M - OH^* + H^+$) (Table I). The separation itself reflects that the photon excitation is instantaneous and further, from a prepared surface where the H$^+$ transfer has already occurred. ΔG_{OH^-} is not invoked in the usual potential-driven OER reaction because the surface is defined at least theoretically by a stable one it approaches at the applied potential[10, 56]. It is important to note that such a surface is not easily followed in time experimentally, since photo-excitation initiates the reaction from a surface defined by an explicit equilibrium with the electrolyte in the dark. While this might seem like a small modification, it is important if one would like to define an initial state of the catalyst from which the O$_2$ evolves especially given that, alongside OER catalysis, the surface often re-structures[57-58]. It is an open question whether a stable form of the heterogeneous catalyst is actually reached in practice and whether that surface can be utilized as the initial starting point of the cycle.

The second way in which the photo-driven OER scheme shown is different is that it is a multi-site mechanism. This may also be the case for a purely potential driven one, given the multitude of available sites (the OER schemes are meant to be reductive so that descriptors can be pulled out) and especially if ΔG_1 is large such that two electron transfers from the same site become prohibitive. For the photo-driven reaction at the semiconductor-liquid interface, holes are also shuttled to the surface efficiently by the built-in electric field (Fig. 7d) such that any available site might trap them; we discuss this charge separation of electron-hole pairs from light more directly with the experiments below in Part IV. Table I utilizes 4 M-OH* [$4(M \cdots O^*, H^+)$] for a proposed, multi-site mechanism by which all the electron transfers occur to separate sites before the bond-forming reaction step. One then bypasses ΔG_2(O*) for which two electron transfers occur to the same site and ΔG_3(O-O) is a purely thermo-chemical step involving the initially created hole-polarons. While differences exist between the multiple and single site schemes, and between the photo-driven and purely voltage-driven mechanisms, ΔG's can still be assigned for the reaction steps. Further, while the photo-induced reaction can be highly driven by a low VB hole potential (positive and large on the RHE scale), it is the relative ΔG's that compare the activity of O$_2$ evolution of different materials.

In order to make a direct connection to the volcano plots, through ΔG_1, one would place the VB edge of semiconductor on the electrochemical scale:

$$\Delta G_1 = VB\ (RHE) + \Delta G_{OH^*}(U_{VB}) \quad (5)$$

This is shown for increasing binding energy of the oxygen in M-OH* with respect to M-OH$_2$ on the band-diagram of STO in Fig. 6d. The H$^+$ transfer of reaction (1) depends on the pH of the solution and the free energy increases with 59 mV/pH on the NHE scale. In utilizing the VB edge, one associates this pH-dependence with the change in the VB edge position due to

hydroxylation; the RHE reference scales with 59 mV/pH which makes this a constant potential. An interfacial dipole (M-OH$^-$) increases the VB edge to more negative potentials in semiconductors and is associated with the innermost screening/Helmholtz layer at the electrode/electrolyte interface[59].

The above has explored how the first electron and proton OER step to create M-OH* can be a predictor of catalytic activity across transition metal oxides and then how one might understand that step at a photo-driven semiconductor/electrolyte interface. The free energy difference for the hole-trapping event, $\Delta G_{OH^*}(U_{VB})$, has been calculated explicitly for a number of semiconductors. The values for TiO$_2$[16] and SrTiO$_3$,[19] along with structural depictions of Ti-OH* in STO, are shown in Figure 8. For each material, several $\Delta G_{OH^*}(U_{VB})$ exist since the hole could trap on lateral as well as terminal sites, with different H$^+$ distributions.

These diverse $\Delta G_{OH^*}(U_{VB})$ of Ti-OH* creation should then lead to new optical and vibrational transitions, as described in Part II. Due to the difficulty of calculating the vertical optical transitions, often this is not attempted explicitly and spectral determinations are made in a generic sense of where they might occur in the UV, visible, and IR. There has been a recent identification of a vibrational transition associated specifically with the Ti-O$^{\bullet-}$ oxyl intermediate on STO. These DFT calculations use a periodic slab of STO with a surface on which water has already dissociated at standard conditions to create water adsorbed and hydroxylated sites[25]. These calculations are shown in Fig. 9, where Fig. 9a depicts the vibrational transitions of the ground state of the slab and that of the oxyl configuration upon hole-transfer. The new mode occurs slightly blue-shifted to the longitudinal optical phonon of the ground state and is associated with the phonon density of states of oxygen right beneath the oxyl. From the point of view of the bonding
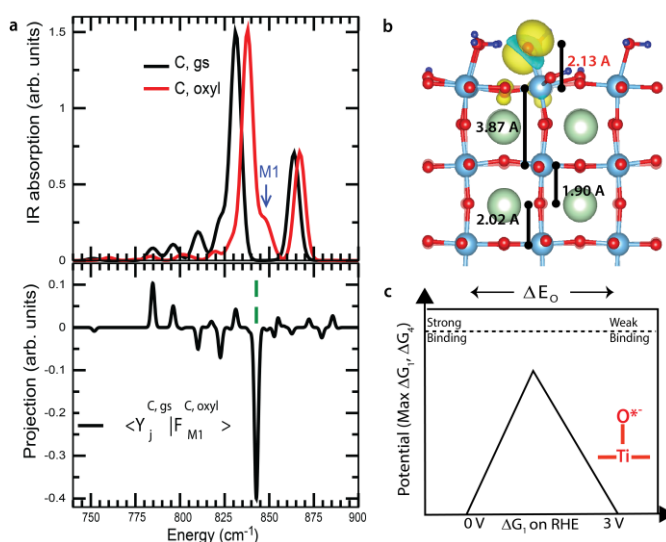
Figure 9: (a) The vibrational infrared absorption associated with a ground state configuration of SrTiO$_3$ and the oxyl surface configuration. Reproduced from ref. 25. (b) Bond distances of the system in oxyl configuration, including the Ti-O surface bond and the two unit cells underneath; the Ti-O bond in the bulk is 1.93 A. (c) The oxyl located approximately on a Volcano plot utilizing the theoretical descriptor, ΔG_1.

configuration, the surface Ti-O bond is extended by 8% upon hole-trapping while the unit cell underneath contracts (Fig. 9b), decoupling the oxygen underneath from the rest of the lattice. Similar bond lengthening is found for both terminal oxyl and lattice bridge configurations in TiO_2.[16] This would then place the oxyl configuration of titania on the weak-binding side of the volcano since the oxygen bonding to the metal is weaker upon hole-trapping (Fig. 9c).

The vibrational transition of the oxyl in STO and its association with a theoretical descriptor of the reaction is a good example of what one would like to achieve using *in-situ* optical and vibrational spectroscopy of OER while isolating the reaction steps in time. In the next section, we delineate the optical and vibrational signatures of M-OH[*] across several transition metal oxides seen to date experimentally and discuss to what extent the connections have been made to relevant theoretical descriptors.

Part IV: The M-OH[*] intermediate during *in-situ* OER by transient vibrational & optical probes

There are three primary challenges to investigating the elementary steps of the OER reaction *in-situ* on the catalytic surface. The first is to have an experimental geometry that is sensitive enough to detect the intermediates. The second is to be able to trigger the catalytic reaction at a distinct time-point, such that the intermediate steps are separable. The third is to be able to differentiate between static changes to the surface, which occur concomitantly with steady state OER in practical catalysts, from the elementary steps.

The primary way that sensitivity to the OER reaction steps by spectroscopy has been achieved to date is to use a change in adsorption associated with the reaction onset. The catalyst is prepared when no reaction takes place, and then the reaction is initiated by light or voltage. The difference in adsorption is then associated with the intermediates. The advantages of this method alone is that it isolates the reaction steps primarily by having all the reaction steps occur spontaneously (*e.g.* Fig. 7a, 7c), such that they are causal. The isolation is then best achieved through a time-dependent probe targeting either the forward or back transfer rates. It can also be achieved by a potential dependence related to the onset of a given reaction step becoming spontaneous; albeit here the interfacial energetics at the solid-liquid interface are altered substantially in the process. These methods are amenable to multi-modal probes, whether or not they are inherently surface sensitive. On the other hand, for the experiment to achieve enough sensitivity, it does depend on how much product change one induces by light or voltage both for the signal-to-noise of the spectroscopic signature and for the isolation of kinetics related to populations of interest from other competing, deleterious reactions. For the transient spectroscopies that directly excite the catalyst and investigate the first OER step, for which the populations of interest are bulk and surface trapped holes, several metrics of the sensitivity include: a quantum efficiency of electron-hole pair separation of light-to-charge conversion, Faradaic efficiency of conversion of charge to final (O_2) product, and the detection level of the probe (~0.1 mOD in ultrafast spectroscopy). Finally, the methods are best at

differentiating intermediates with substantially modified bonding structure, such as local, polaron distortions from bulk, delocalized holes. When combined with a more surface sensitive technique (*e.g.* sum-frequency generation or grazing incidence reflection), or detected as a function of higher surface to volume in nanoparticles, surface intermediates with subtler changes compared to the bulk would be better detected.
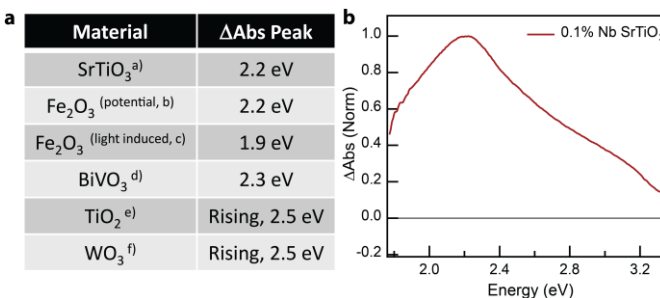
Separating the reaction steps in time has only been achieved by combining the initiation of the spontaneous chemical reaction with a transient pump-probe spectroscopy where time delays between the pump and the probe investigate sequential reaction steps. This is suggested by the free energy diagram of Fig. 7c, where after light initiation all the reaction steps are downhill and one can probe each sequentially in time, provided there is enough time resolution. The time resolution in the techniques varies by a lot, ranging from 100's of femtoseconds[19, 25-26, 60-61] to milliseconds[30-31, 33-34, 62-64]. The time resolution depends not only on the pump and probe pulse temporal duration, but also on the synchronicity with which the catalysis is initiated. For example, when excited by a dye in solution with nanoparticles[31-32], the diffusion time will delay the start of the reaction, and can convolve reaction steps especially if the pump is not synchronous with a new batch of catalyst. For an n-doped semiconductor-liquid interface[19, 25, 27, 29, 60, 62-65], this timing is controlled by the built-in electric field that separates electron-hole pairs; as an example, the charge-separation step for a ~0.05 V/nm electric field is within 100's of femtoseconds for mobile carriers in TMO semiconductors. While the millisecond techniques are sensitive to the buildup of intermediates allowed by the accumulated reaction steps, a true ultrafast initiation of the reaction and ultrafast probe that ranges in time promises to isolate the steps individually. Further, by truly isolating the steps in time, the sensitivity of the spectroscopy to each intermediate should improve. It is also by isolating the kinetics by time-resolution that one can truly investigate individual reaction steps as a function of pH, salt concentration, isotope exchange, and temperature.

Finally, there are two essential ways to perform the spectroscopy while considering the effects of surface re-structuring during catalysis. For pristine, single crystal samples for which one generally does a reflectance measurement, one can scan the surface during data taking at faster and faster rates until the static changes do not affect the reflectance change, $\Delta R (t)$. In certain cases, as will be delineated in upcoming publications on $SrTiO_3$[66], this continual scan does converge to a nominally clean surface at a fast enough speed, which can be tested by $\Delta R (t)$ and the broadband probe spectra. For nanoparticle samples excited by a dye in solution, data can be taken only after the first pump pulse[32, 34], replenishing the sample for subsequent pulses to collect enough signal to noise. While the time-resolution is limited by both the diffusive dye and how fast the sample can be replenished, the method allows for a synchronicity of reaction steps with the pump-trigger.

Transient Attenuated Total Reflection Infrared Spectroscopy: The following section reports briefly on the recent experiments that detect the vibrational levels of M-OH[*] using an evanescent, mid-infrared probe beam. The propagating beam in the ultrafast experiments originates from an optical parametric amplifier (OPA)

and a 1 kHz, 800 nm, 150 fs seed pulse. In the millisecond and static experiments, the probe is interferometric in an FTIR system. All of these beams become evanescent, or decaying, in an attenuated total reflection (ATR) cell which uses internal reflection at a crystal interface to create the decaying wave. If the interface is nanoparticles in solution, the evanescent wave probes all of the nanoparticles within its spatial decay[31]. If the interface is the electrolyte, the evanescent wave probes the electrolyte first and then the electrolyte/electrode interface which is at a distance from the ATR crystal[25, 27]. These two essential experimental geometries are diagrammed in Fig. 10a. For the evanescent wave that probes the electrolyte first, there are also two different samples used for the electrode/electrolyte interface—one being a thin film[27], and the other a bulk crystal sample[25]. These are differentiated since the evanescent wave can interfere with itself by reflecting at the boundaries of the thin film, while it cannot in a bulk crystal sample. The effect of this is that one can be sensitive to bulk, phonon modes through the interference in the thin film.

Here, we summarize the main observations of the vibrational levels of a site-specific M-OH* across TMOs thus far using the infrared evanescent wave generated by ATR (see Table in Fig. 10b). The first observation was made by Frei $et.$ $al.$[31] on the Co=O oxo intermediate in Co_3O_4 at 840 cm^{-1} for which isotope O^{16}/O^{18} and H/D exchange identified a new double bond upon hole-trapping and one in which the H^+ was not explicitly bound (Fig. 10c). These used nanoparticles in solution, to which charge was transferred by photo-excitation of the $Ru(bpy)_3$ dye in the presence of a sacrificial reagent (persulfate). A similar observation was made later for the Fe=O in Fe_2O_3 at 898 cm^{-1} also using isotope exchange, but the thin-film geometry and with potential rather than light excitation (Fig 10c)[27]. The first ultrafast experiments identified the Ti-O$^{•-}$ oxyl intermediate on the STO bulk crystal surface at 795 cm^{-1} using efficient band-gap excitation of the photo-diode at the STO/electrolyte interface[25]. The mode assignment, achieved through the detailed DFT calculations shown in Part III, is that of a sub-surface mode not expected to shift with surface isotope exchange. It was identified as an interfacial mode using a Fano resonance, which is a coupling of a sharp mode

Material	ΔAbs Peak
SrTiO$_3$[a)]	2.2 eV
Fe$_2$O$_3$ [(potential, b)]	2.2 eV
Fe$_2$O$_3$ [(light induced, c)]	1.9 eV
BiVO$_3$[d)]	2.3 eV
TiO$_2$[e)]	Rising, 2.5 eV
WO$_3$[f)]	Rising, 2.5 eV

Figure 11: (a) The peak of the positive change in absorption during OER in different 3d TMOs, from a-ref. 19, 66, b-ref.29, c-ref. 63, d-ref. 65, e-ref. 64, f-ref. 62 (b) An example spectrum of the change in absorption for SrTiO$_3$ (0.1% Nb)

to nearby continuum density of states. In particular, the mode couples to plasma excitations in the solid and rotational-vibrational transitions in the water (librations), which are modulated by n-doping density and Hydrogen/Deuterium exchange respectively (Fig. 10d). The quantum efficiency of light to charge varies for the different oxides and experimental conditions, with about 10% for the hematite electrode under continuous illumination, while it is above 75% for the STO electrode under pulsed, ultrafast experiments. In the ultrafast experiments, this increased efficiency helps extract the time-evolution of the intermediate population, as will be described below. In the nanoparticle experiments initiated by $Ru(bpy)_3$, while the overall efficiency of light to O_2 production is not reported given that the dye and not the electrode initiates the reaction, the O_2 evolution is reported directly by a Clark electrode, with the amount of O_2 produced linearly dependent on the duration of the light pulse. The STO experiments also report an efficiency of charge to O_2 production by a Clark electrode, which is approximately Faradaic with error bars of +- 20%[60].

Two other recent assignments of the charge-transfer intermediates of OER have been made, in layered hydroxide materials, one concerning MnO_x[36] and the other a NiFe[35] hydroxide (NiFe-LDF). Both are associated with three electron transfers and one proton transfer prior to O_2 evolution. They include high oxidation states of the active metal (Fe(VI) and Mn(VII)) along with
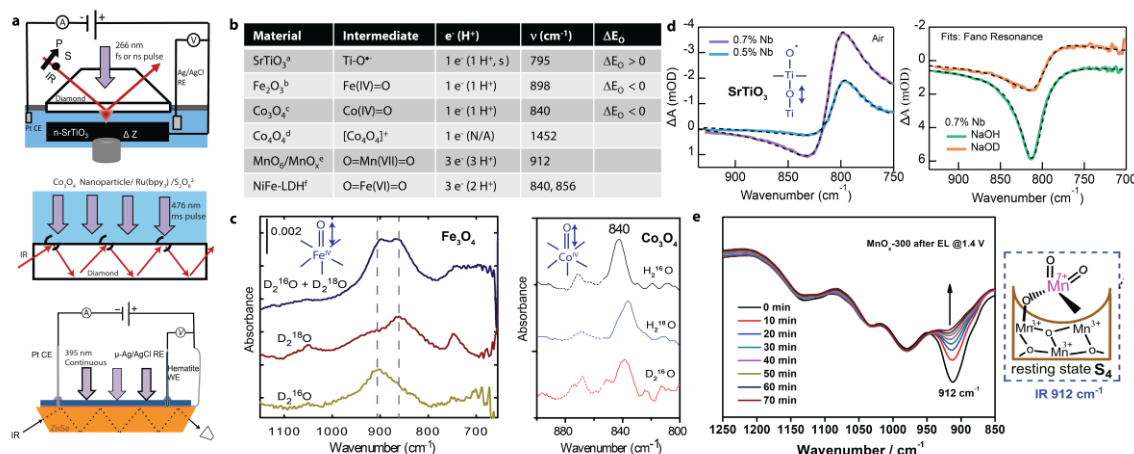
Figure 10: (a)ATR-IR configurations for driving and probing O_2 evolution on SrTiO$_3$ (top), Co$_3$O$_4$/Ru(bpy)$_3$ (middle), and Fe$_2$O$_3$ (bottom). (b) Table of vibrational frequencies associated with the M-OH* intermediate prior to O-O bond formation, from a-ref. 25, b-ref. 27, c-ref. 31, d.-ref. 30, e-ref. 36, f-ref. 35. (c) Fe(IV)=O and Co(IV)=O vibrational spectra on Fe$_2$O$_3$ and Co$_3$O$_4$ reprinted with permission from Springer Nature: Nat $Chem$ 8 (8), 778-83, 2016 and Nat $Chem$ 6 (4), 362-7, 2014 respectively. (d) The sub-surface vibration of Ti-O$^{•-}$ on SrTiO$_3$ reproduced from ref. 25. The spectral changes associated with two different n-dopings and upon H/D exchange fit by a Fano resonance between the vibration and the continuua are shown. (e)The symmetric tetrahedral vibration of the O=Mn(VII)=O complex reproduced from ref. 36 (open access journal).

the formation of two terminal oxo bonds to the metal site; the 912 cm^{-1} vibration, shown in Fig. 9e as a function of time after the reaction was stopped, is assigned to an anti-symmetric stretching frequency of a tetrahedral MnO_4^- configuration. While not assigned to the first electron and proton transfer, the charge-transfer intermediates should also occur prior to the purported O-O bond-formation step. Furthermore, for the MnO_x layered hydroxide, it is suggested that the 3-electron intermediate arises from pooling 1-electron intermediates in the interior of the compound. On the other hand, there are clear peaks in the cyclic voltammetry for the NiFe-LDF which lead the authors to suggest three successive electron transfers to the terminal sites. These studies were done in a non-aqueous solution, which could change the environment of how the charge is pooled to create the reactive intermediate prior to O_2 evolution.

Finally, the M-OH* intermediate was also reported in a molecular compound, Co_4O_4.[30] A doublet, 702 and 694 cm^{-1} associated Co-O stretches, appears as a result of the 1-electron oxidation of the cubane, shifted from the ground state Co-O stretches. The result suggests a more delocalized form of M-OH* across all four metal sites of the cubane, rather than the localized oxo (Co=O) in the extended Co_3O_4 solid. X-ray absorption spectroscopy in the CoPi catalyst also suggest a cubane form relevant to the intermediate steps of OER[67-69].

We now suggest a way to map the structure of these intermediates to a relevant theoretical descriptor, the change in binding energy of the oxygen upon the first electron and proton transfer. In the iron and cobalt oxo's, a double bond is formed upon hole trapping which would be a shortening of the bond compared to the native bonds in the oxide and to any terminal hydroxylated and water absorbed groups. This suggests that, in these oxides, ΔG_1 lies on the strong-binding side of the volcano. On the other hand, in STO, it is found that the Ti-O bond in the titanium oxyl lengthens significantly (8%) compared to a hydroxylated site. This suggests then, for the oxyl, ΔG_1 lies on the weak-binding side of the volcano. Based on the information available in the manuscripts, and the complication of understanding the double oxo bonds compared to the bulk, we confine our assignments to these few compounds. The three do suggest oxygen binding within ΔG_1 to be a relevant descriptor and give some indication on which side of the volcano each of the materials lie.

To further these assessments, structural determination of these intermediates and the associated ΔG_1 and $\Delta G_{OH*}(U_{VB})$ by calculation are highly desired. Implicit in the comparisons is also the need to obtain the driven catalytic surface with the same excitation technique across material surfaces. Ideally, this would be an ultrafast technique that could detect the intermediates at a range of time-scales, such that the meta-stable coverage of M-OH* could be related to forward and back transfer rate constants as delineated in Part II.

Transient Optical Spectroscopy: As described above, polaronic distortions of the M-OH* intermediates lead to both new emissive and absorptive transitions arising from a population of M-OH*. Here, we experimentally identify the absorptive and emissive transitions seen.

The absorption change generally occurs as a positive peak in the range of 2 eV, as shown by the table in Figure 11a. As an example, the change in absorption for 0.1% Nb $SrTiO_3$[19, 66] upon ultrafast band-gap excitation are reproduced in Figure 11b. This approximately ~ 1 eV wide absorption at ~2 eV is also seen in Fe_2O_3[63] and $BiVO_3$[65] upon band-gap excitation pulse of seconds duration and reported with millisecond time pulse has been turned off. The photo-induced absorption has also been recorded for TiO_2[64] and WO_3[62] albeit with a rise towards 500 nm rather than a discernable peak. While the quantum efficiency of light to charge conversion in the $SrTiO_3$ experiments is large > 75%[60], the near steady-state experiments are conducted under an efficiency of a couple percent (2—3%)[62-63]; there, correlations of the absorption change are made also with potential. Finally, the induced absorption in Fe_2O_3[29, 71] is also measured as a positive ΔmOD upon band-gap light excitation, but as a difference of the photo-induced change at two potentials, during steady state O_2 evolution and without. This potential-induced absorption change exhibits similarities to the absorption change between two molecular analogues of the ground and excited state surfaces, Fe(V)B*=O with respect to Fe(III)B*(H_2O). It also coincides with the existence of a trapped state on the surface, identified by electrochemical impedance measurements.
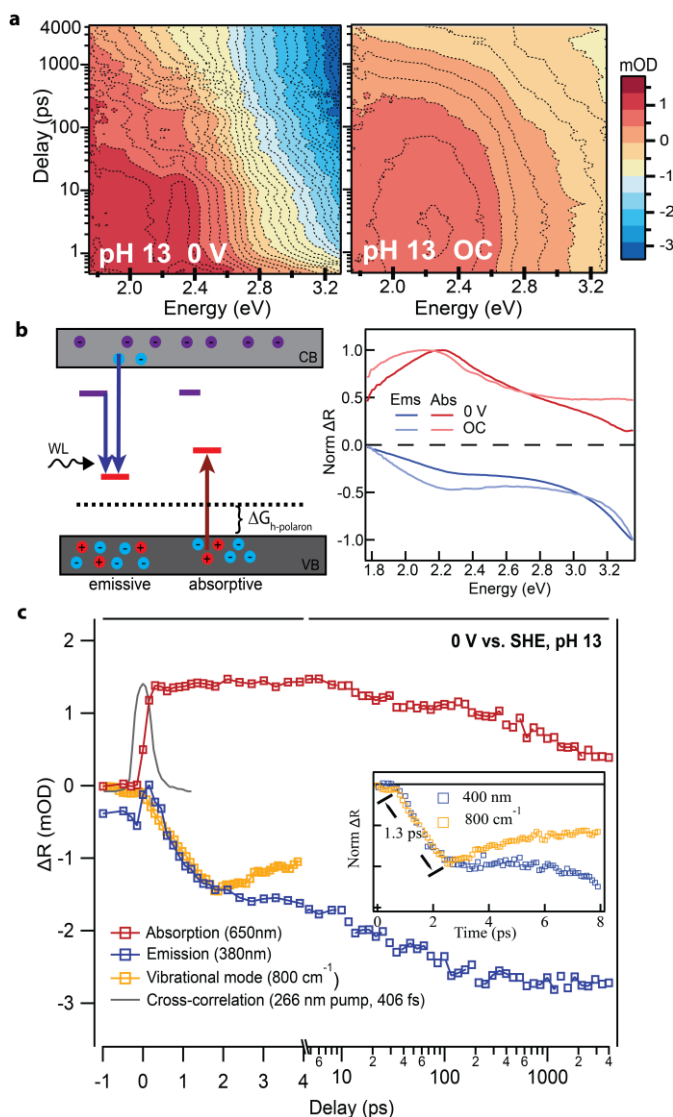
Figure 12: (a) Time-energy spectra of the n-SrTiO₃/aqueous interface by ultrafast broad-band optical spectroscopy that initiates efficient catalysis for both closed circuit (top, 0 V vs. SCE) and open circuit (bottom, OC) in pH 13. (b) Emissive and absorptive spectra obtained through a principle component analysis of optical spectra such as that shown in (a) across a range of pH and salt concentrations. OC and 0 V are shown. (c) Transient traces of the absorption at 650 nm (red) and emission at 380 nm (blue) in closed circuit. The transient trace of the oxyl's sub-surface vibration is overlapped (yellow). The gray pulse is the cross-correlation of the pump beam (266 nm) with an 800 nm probe that shows a time-resolution of 406 fs. Inset shows the 0-8 ps emission probed with a single wavelength, 400 nm beam to compare directly with the mid-infrared trace of the oxyl at 800 cm⁻¹, from which the formation time is determined to be 1.3 ps. The time-trace is reproduced from ref. 19.

Given the broadness of the UV-VIS transitions and that a clear peak in the visible exists only for some, the absorptive transition of the hole-polaron PES will co-exist with intraband transitions of the VB and for the visibly excited materials (Fe_2O_3 and $BiVO_3$) with the band-gap transition. Here, we focus on the contribution involving the hole-polaron PES given the theoretical framework (Fig. 4). The initial state consists of a hole-polaron and a VB electron, both at $R_{polaron}$, while the final state consists of a vibrational excitation of the photo-excited PES. The spectral shape would be that of the hole-polaron density of states (DOS) only for a completely delocalized VB

of O 2p character and for a hole-polaron with a fairly deep well at the distorted reaction coordinate; the peak in the absorptive transition would occur at an energy defined by the difference between the electronic component of ΔG_{OH*} in the hole-polaron PES and the VB edge. However, calculations of the vertical optical transitions[11, 16, 51] suggest that they do not correlate in such a facile manner with ΔG_{OH*}, which emphasizes the importance of the excited vibrational final state as diagrammed in Figure 4. Experimentally, the assignment of the absorptive spectrum to a population has varied, relying predominantly on experimental correlations. For Fe_2O_3, the hole-polaron DOS is emphasized due to the correlation between the absorptive transitions and the trap states in the electrochemical impedance[29], while the VB hole density of states is emphasized in the pump-probe spectroscopy of $SrTiO_3$[19, 61] and Fe_2O_3,[63] largely based on the fluence dependence.

On the other hand, emissive transitions should also appear due to hole-polarons. In the context of OER, these have been discussed with regard to lightly n-doped (0.1% Nb) $SrTiO_3$ for which the initial surface at neutral pH is partially hydroxylated[47]; the Ti-OH⁻ then constitute dilute defects within the water network. In these experiments[19, 66], a broader band white light source (380 nm to 700 nm) is utilized, and both the absorptive and emissive transitions are tracked from ultrafast time-scales. Representative optical spectra are shown in Figure 12 for 0.1% Nb STO for open circuit and closed circuit conditions. The emissive transition (blue) occurs at the more UV end of the spectrum, but overlaps with the absorptive transition within the window. Both absorptive and emissive transitions occur during steady state O_2 evolution (closed circuit, CC) and when the current response is transient (open circuit, OC). Representative spectra obtained through a principle component analysis are shown for both OC and CC (Fig. 12b). The advantage of the ultrafast spectroscopy is that now the time-evolution of the populations contributing to each transition can be followed from their inception. In Figure 12c, this is shown for the red, absorptive end of the spectrum, and the blue, emissive end of the spectrum. The absorptive transition arises within the pump-pulse duration (406 fs) and then decays, while the emissive transition arises with a distinct and longer time scale (1.3 ps) followed by another rise (~60 ps) and then levels off on the nanosecond time-scale. The 1.3 ps rise, furthermore, occurs also in the vibrational transition that follows the oxyl's sub-surface mode after pump excitation. That such a structural assignment has been made to the emissive, optical transitions associated with trapped holes is unique; the comparison, reproduce from ref.[19], is shown in the inset of Fig. 12c. This 1.3 ps rise is the forward transfer rate (k_f) for polaron formation discussed in Part II with Marcus Theory. That it is fast reflects a nearly activation-less barrier at the semiconductor-liquid interface.

The time evolution of the emissive response primarily follows the time-evolution of the trapped hole-polaron population. This is evident from the appearance of a growth, as expected for an exothermic ΔG_{OH*}, and the distinct time-scale associated with it. For the emissive transition, the initial state consists of a hole-polaron and a CB electron at $R_{polaron}$ coordinate, while the final state consists of a vibrational excitation of the ground state PES. Here, one again might not expect the spectra to track the hole-polaron DOS because of the vibrational excitations involved, especially considering a fairly localized CB in many 3d transition metal oxides. For STO, a small -ΔG
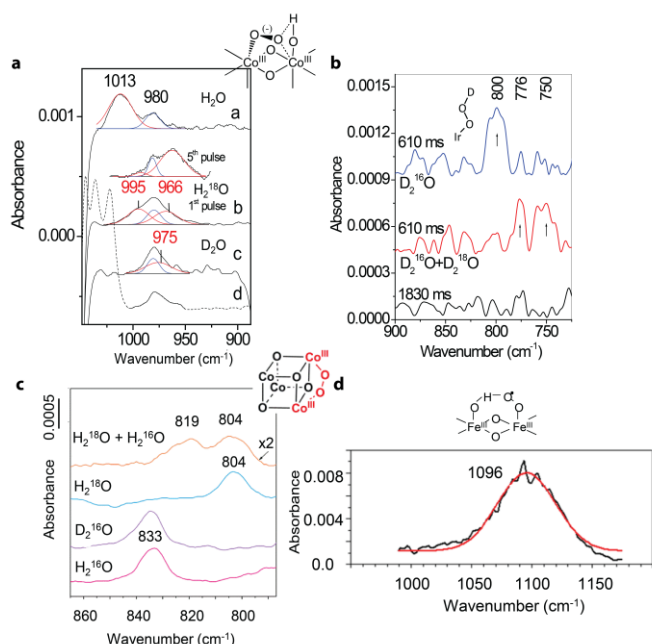
of 0.05 eV for bulk hole-polarons leads to an emissive transition at 2.5 eV rather than near 3.2 eV, the band gap energy[51]. On the other hand, since the transition arises from conduction band states (*e.g.* dopant or photo-excited electrons) that do not contribute to creating hole-polarons, the time-evolution of the CB electrons is then confined to charge separation (~100 fs) and electron-hole recombination mitigated by the high quantum efficiency (> 75%), such that the 1.3 ps associated with $\Delta G_{OH*}(U_{VB})$ is observed. In contrast, the appearance of the absorptive transition within the pulse duration identifies that it occurs with the creation of free carriers. While this suggests that VB holes are followed largely by the absorptive transition, given that the VB density of states is being utilized to create the hole-polarons and the large population of VB holes induced by the laser pulse, one might consider that the time-evolution of the absorptive transition is a complex function of the VB hole and hole-polaron populations.

The absorptive and emissive transitions are quite broad and this has several possible origins other than that they involve vibrational excitations. In particular for OER, different structures of M-OH* exist, as elucidated above; each species would have a unique transition. Furthermore, these species have been calculated to interconvert on picoseconds time-scales by ab-initio molecular dynamics[16, 72]. This diffusive interconversion would then associate the optical transitions not with a distinct population of hole-polarons but the total M-OH* on the surface involved in the interconversion at each reported time-scale. Finally, intra-band transitions and changes in the refractive index could also contribute to the broadening. For the emissive transition, there is a rise near the band-gap energy

Figure 13: Vibrational spectra of the O-O bond as a function of O^{16}/O^{18} and H/D exchange for a) Co_3O_4 (reprinted with permission from Nature Springer: *Nat Chem* **6** (4), 362-7, 2014), b) IrO_2 (reprinted (adapted) with permission from *Journal of the American Chemical Society* **133** (33), 12976-12979. Copyright (2011) American Chemical Society), c) Co_4O_4 (reprinted (adapted) with permission from *ACS Catalysis*, **10** (3), 2138-2147. Copyright (2020) American Chemical Society), and d) Fe_2O_3 (reprinted (adapted) with permission from *Journal of the American Chemical Society*, **140** (9), 3264-3269.. Copyright (2018) American Chemical Society), reproduced from the references noted. a), b), and c) were driven by Ru(bpy)$_3$ while d) utilized a band-gap excitation. All were probed by FTIR.

which could either be associated with the occupation of the rising density of states at the CB edge by n-dopants or a change in the refractive index.

It is also important to take into account that laser initiated catalysis heats the sample and how this heat could affect the signal of especially the optical probe. The heating itself largely arises from thermalization of carriers to the band gap edges, in the case of above band-gap excitation and a high quantum efficiency for charge separation, and full carrier recombination across the band-gap, in the case of a low quantum efficiency. Estimates can be made for the average temperature rise utilizing the laser fluence, the excited volume, the excitation wavelength, the quantum efficiency, and the specific heat of the sample. For low fluences (< 0.04 mJ/cm²), the average temperature rise is a couple of K even under conditions of low QE[70]. While this does not appreciably affect the thermodynamic and kinetic constants per se, it could manifest in changes in the optical spectra, such that they are not simply relatable to populations of holes and hole-polarons. As reviewed previously[70], this has been addressed by: 1) Identifying the spectral change heating induces and estimating its contribution, 2) Utilizing voltage to increase the quantum efficiency and decrease electron-hole recombination, 3) Utilizing chemical scavengers to diagnose whether the signal dominantly relates to hole-trapped species. For 3), the spectra's dependence on fluence is also a diagnostic, since it could identify a saturation of chemical species in a surface limited reaction. Overall, decreasing the laser fluence is a facile and general practice that minimizes heating effects. Another way to minimize heating effects specifically for reactions run under a high QE is to excite near enough to the band gap edge, such that less thermalization results. We note that the effects of heating will be more prominent for optical spectra of electronic transitions due to the refractive index changes involved; vibrational transitions will be subject to heating only to the extent that their anharmoncity changes within 10's of K.

It would be quite important to substantiate spectral assignments by quantum mechanical calculations of the vertical transitions associated with ΔG_{OH*}. Complementarily, both emissive and absorptive transitions should be tracked across material surfaces. Finally, ab-initio molecular dynamics simulations of the time-constants associated with ΔG_{OH*} are highly desirable. As just discussed, the time constant for interconversion has been calculated on aqueous TiO_2. On the other hand, the time-scale of hole-trapping reported experimentally as 1.3 ps on 0.1% Nb STO has not been calculated to our knowledge. Such calculations on a range of transition metal oxide materials, in conjunction with the further experimental work, would substantiate the assignment of these emissive and absorptive transitions and broaden their utility in following the electron-transfer intermediates of water oxidation.

Experimental observations of the structure and kinetics of O-O Bond Formation: The meta-stable M-OH* intermediates should give rise to the O-O bond, either after further electron transfers, or by diffusing across the surface, pooling the charge into two or three-electron intermediates. We first highlight the recent structural determinations of the O-O bond by ATR-FTIR vibrational spectroscopy. Figure 13 shows determination of the O-O bond on several transition metal oxides. The reports on IrO_2,[73] Co_3O_4,[31] and the molecular cubane Co_4O_4[30] come from work by Heinz Frei *et. al.*

The report on Fe_2O_3, comes from Jincao Zhao et. al.[74] All of the spectroscopic measurements utilize the ATR-FTIR cells depicted in Fig. 9. The work by Heinz Frei initiates the catalysis on nanoparticles by a single ~100's ms excitation pulse of Ru(bpy)₃ in the presence of a sacrificial reagent; the work by Jincao Zhao utilizes steady state excitation of a nanowire electrode. H/D and O^{16}/O^{18} exchange is utilized to identify the O-O bond itself and associate more detailed structural information on how it binds to the surface, as depicted in the cartoons.

The identification of a meta-stable O-O bond on a variety of surfaces, in conjunction with experimental data on the meta-stable

concentration shows a direct exchange between one pathway and another implicates the thickness of the screening layer in bifurcating the pathways (Fig. 14c). The report also discusses how transition state theory can be applied to understand these reaction kinetics, following changes in the activation barrier height (~0.4-0.5 eV) with both temperature and salt concentration/ionic strength (Fig. 14d). One of the proposed reaction pathways, based on the picosecond rise of the Ti-OH* population followed by the microsecond decay is that of four electron transfers creating four Ti-OH* followed by dark, thermochemical steps that guide the formation of the O-O bond and O_2 release; this is the multi-site, photo-driven mechanism shown in
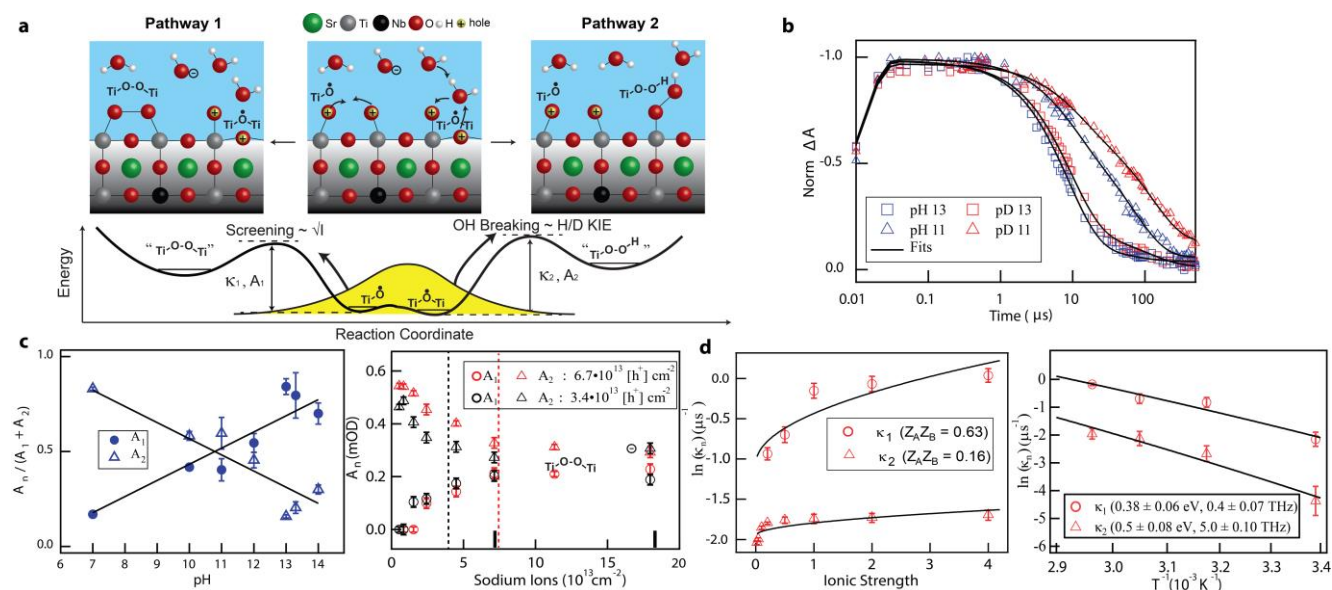
Figure 14: Microsecond bond formation kinetics revealed by an optical probe of the SrTiO₃/aqueous surface during O₂ evolution. a) Cartoon of diffusing Ti-OH* intermediates reaching two separate activation barriers to form the purported transition states. b) Exemplary transient traces of the emissive transition probed at 400 nm, and as a function of pH and H/D exchange. c) Pathway dependence between the two activation barriers as a function of pH and salt concentration, with the faster route favored at higher pH (blue) and salt concentration (black/red for two different fluences). The H/D KIE of b) is 1.8 on the slower time constant. d) Rate constants of the two pathways as a function of ionic strength and temperature. Time constants at pH 13 are 8 μs and 60 μs for pathway 1 and pathway 2 respectively. The temperature dependence reveals activation barriers in the range of 0.4-0.5 eV. Figures reproduced from ref. 38.

M-OH* intermediates, suggests that one could in principle time resolve the formation of the O-O bond from the first OER intermediates. To date, this has been attempted most directly by following the decay of the Ti-OH* population by its emissive transitions on SrTiO₃ with a 400 nm probe from nanoseconds to microseconds. Figure 14 shows work reproduced from ref.[38] where two distinctive time-constants identify two parallel decay pathways (Fig. 14a and 14b). The population going through each pathway is highly dependent on the reaction conditions, such that the faster 6 μs pathway is favored at higher pH and salt concentration/ionic strength while the slower 80 μs pathway is favored at lower pH and salt concentration/ionic strength (Fig. 14c). The slower pathway exhibits a distinct H/D kinetic isotope effect of 1.75 (Fig. 14b). Based on the two pathways, two different types of O-O bond, one originating from oxyl radical recombination and another from nucleophilic attack of the lattice oxygen are proposed (Fig. 14a). As diagrammed, the activation barriers are reached by a diffusing surface population of geometrically diverse one-electron, Ti-OH* intermediates. Indeed, the distinctive decay kinetics observed support the idea that the total population of Ti-OH* is targeted by the optical emission. Further, that the dependence on the salt

Table I. It is important to note in this context that the 60 ps rise in the optical emission is not clearly assigned yet.

These experiments suggest that indeed the catalytic cycle is resolvable in time utilizing optical and vibrational probes. The relevance of reaction conditions in identifying a transition state further suggests an as yet unexplored option to define the reaction pathway. As brought up in Part II, if meta-stable intermediates do guide the spontaneous reaction, one should be able to separate the reaction steps by effective equilibrium constants that define the separate ΔG associated with the minima in the intermediate PES's (e.g. Fig. 1). The way to obtain these equilibrium constants experimentally is to shift the concentrations of the reactants by the reaction conditions. For example, one could shift the hydroxylation of the surface to obtain more ground state M-OH⁻ (reaction (1)) which would then lead to more meta-stable M-OH* (reaction (2)) at the same surface excitation. Another option is to increase the surface excitation (e.g. by the laser fluence) to create more M-OH* which would then shift the equilibrium towards the O-O bond.

Part V: Future experimental & theoretical studies of the hole-polaron within OER:

In this concluding section, we highlight recommendations for future work in this area which follow from the delineation of the polaron's conceptual framework, its spectral signatures, its relevance to OER, and its observation in real systems. The recommendations range from most immediate, arising directly from the recent experiments, to farther in the future, given what could become accessible. They are:

- A full time-evolution of the M-OH* population on diverse 3d TMO's from picoseconds through milliseconds using optical and vibrational probes. While the community has observed these OER intermediates, the experimental time-range for each material varies immensely. It would be important to know at which time-scale the largest meta-stable population exists for each 3d TMO to extract forward (k_f) and back transfer (k_b) rates. Further, these kinetics could further adjudicate the relevance of surface diffusion to OER and of multiple, distinct OER pathways.

- Quantum mechanical calculations of hole-trapping at the 3d TMO/aqueous interface are desired in the following areas: a) Detailed structural forms of M-OH* coinciding with ΔG_{OH*} b) Time-scales of M-OH* formation, which has yet to be calculated, and of interconversion between different geometric forms of M-OH*, c) The vertical optical transitions between the M-OH* population to both CB and VB states. These mid-gap transitions are easily followed experimentally, and likely represent the sum of the total population of M-OH* in multiple geometries, thereby targeting the average kinetics of the reaction steps.

- To truly identify the reaction steps, their transition states and equilibria should be modulated by reaction conditions and the time-dependence of the individual reactant and product populations followed. This would be key to connecting time-resolved spectroscopy, inherently kinetic, to either the thermodynamic free energy differences of the reaction steps (chemical equilibria) or the thermodynamic state at the top of the barrier (transition state theory).

- While optical and mid-infrared vibrational spectroscopy alone have been quite informative, new probes of the interface are desired. In particular, those that can separate out the geometries of M-OH*, are sensitive to the O-O bond configuration, and that can ideally, follow the surrounding vibrational structure as the O-O bond evolves out of M-OH*. Two proposed spectroscopies are femtosecond stimulated resonance Raman spectroscopy, which would be particularly sensitive to the vibrational structure of intermediates and the O-O bond, and X-ray absorption spectroscopy, which would be particularly sensitive to the bond-distortions themselves. This recommendation has the caveat that all of these spectroscopies target intermediates with localized electronic structures; the more delocalized the charges become, the more the multi-modal techniques will have to work together to identify them.

- It is becoming apparent that information on the ultrafast time scale is quite relevant to catalysis, in that it reports on the formation kinetics of the first OER reaction step. The next challenge would be to understand the dynamics behind these kinetics, such as energy released to lattice strain, plasmon excitations, or to the rotational-vibrational modes of water, all within the context of the Helmholtz screening layer. To target the coupling of the formation of M-OH* to the environment, coherent spectroscopies are desired, with two-dimensional optical and vibrational spectroscopy being the direct analogues to those spectroscopies presented here.

- These methods may also be translatable to other electrochemical oxidative reactions in aqueous electrolyte that involve TMO surfaces and surface-bound, reactive oxygen intermediates. Two examples are CH_3OH oxidation to various products and CO oxidation to CO_2. Methanol oxidation takes place readily on TMO surfaces with a methoxy species, M-O*-CH_3, as a primary intermediate resulting from M-OH*. While CO oxidation occurs on TMO surfaces, it does so more readily on noble metal surfaces. On the other hand, a generally proposed intermediate of CO oxidation is the adsorbed O* ad-atom on a metal site, which in aqueous solutions would likely be created by electron transfers from water.

Conclusions

The perspective gives a tutorial on how bound hole-polarons relate to the electron-transfer intermediates of OER (M-OH*), and reviews recent kinetic and structural information obtained from optical and vibrational spectra of them during *in-situ* photo-electrochemically driven OER. These data have the potential to measure thermodynamic quantities, such as the free energy differences upon proton and electron transfer (*e.g.*, ΔG_1) and activation free energies of the catalytic cycle, that were previously accessible exclusively through theoretical calculations. They also suggest that time-resolved spectroscopy of the OER reaction can indeed isolate reaction steps, with the formation of the O-O bond from the M-OH* intermediates a clear target for future investigations.

Author Contributions

The corresponding author, T. Cuk, wrote the article with the input of H. Lyle, S. Singh, M. Paolino, and I. Vinogradov.

Conflicts of interest

"There are no conflicts to declare".

Acknowledgements

of Energy at RASEI (Boulder, CO) under Contract No. DE-SC0018939.

Notes and references

1. Banin, U.; Waiskopf, N.; Hammarstrom, L.; Boschloo, G.; Freitag, M.; Johansson, E. M. J.; Sa, J.; Tian, H.; Johnston, M. B.; Herz, L. M.; Milot, R. L.; Kanatzidis, M. G.; Ke, W.; Spanopoulos, I.; Kohlstedt, K. L.; Schatz, G. C.; Lewis, N.; Meyer, T.; Nozik, A. J.; Beard, M. C.; Armstrong, F.; Megarity, C. F.; Schmuttenmaer, C. A.; Batista, V. S.; Brudvig, G. W., Nanotechnology for catalysis and solar energy conversion. *Nanotechnology* **2021,** *32* (4).

2. Hammarstrom, L.; Hammes-Schiffer, S., Artificial Photosynthesis and Solar Fuels. *Accounts of Chemical Research* **2009,** *42* (12), 1859-1860.

3. Markovic, N. M., Electrocatalysis: Interfacing electrochemistry. *Nature materials* **2013,** *12* (2), 101-2.

4. Hammes-Schiffer, S., Proton-Coupled Electron Transfer: Moving Together and Charging Forward. *Journal of the American Chemical Society* **2015,** *137* (28), 8860-8871.

5. Hammes-Schiffer, S.; Stuchebrukhov, A. A., Theory of Coupled Electron and Proton Transfer Reactions. *Chemical Reviews* **2010,** *110* (12), 6939-6960.

6. Kern, J.; Chatterjee, R.; Young, I. D.; Fuller, F. D.; Lassalle, L.; Ibrahim, M.; Gul, S.; Fransson, T.; Brewster, A. S.; Alonso-Mori, R.; Hussein, R.; Zhang, M.; Douthit, L.; de Lichtenberg, C.; Cheah, M. H.; Shevela, D.; Wersig, J.; Seuffert, I.; Sokaras, D.; Pastor, E.; Weninger, C.; Kroll, T.; Sierra, R. G.; Aller, P.; Butryn, A.; Orville, A. M.; Liang, M.; Batyuk, A.; Koglin, J. E.; Carbajo, S.; Boutet, S.; Moriarty, N. W.; Holton, J. M.; Dobbek, H.; Adams, P. D.; Bergmann, U.; Sauter, N. K.; Zouni, A.; Messinger, J.; Yano, J.; Yachandra, V. K., Structures of the intermediates of Kok's photosynthetic water oxidation clock. *Nature* **2018,** *563* (7731), 421-425.

7. Seh, Z. W.; Kibsgaard, J.; Dickens, C. F.; Chorkendorff, I.; Norskov, J. K.; Jaramillo, T. F., Combining theory and experiment in electrocatalysis: Insights into materials design. *Science* **2017,** *355* (6321).

8. Pegis, M. L.; Wise, C. F.; Martin, D. J.; Mayer, J. M., Oxygen Reduction by Homogeneous Molecular Catalysts and Electrocatalysts. *Chemical Reviews* **2018,** *118* (5), 2340-2391.

9. Busch, M.; Halck, N. B.; Kramm, U. I.; Siahrostami, S.; Krtil, P.; Rossmeisl, J., Beyond the top of the volcano? – A unified approach to electrocatalytic oxygen reduction and oxygen evolution. *Nano Energy* **2016,** *29*, 126-135.

10. Rossmeisl, J.; Qu, Z. W.; Zhu, H.; Kroes, G. J.; Nørskov, J. K., Electrolysis of water on oxide surfaces. *Journal of Electroanalytical Chemistry* **2007,** *607* (1-2), 83-89.

11. Schirmer, O. F., O–bound small polarons in oxide materials. *Journal of Physics: Condensed Matter* **2006,** *18* (43), R667-R704.

12. Austin, I. G.; Mott, N. F., Polarons in crystalline and non-crystalline materials. *Advances in Physics* **2001,** *50* (7), 757-812.

13. Wu, K.; Lin, S.; Luo, C.; Uen, T.; Lin, J.-Y.; Juang, J.-Y., Polaron Dynamics and Coherent Acoustic Phonons in La 0.45 Ca 0.55 MnO 3 Thin Films Studied by Ultrafast Pump-Probe Spectroscopy. *Journal of Superconductivity and Novel Magnetism - J SUPERCOND NOV MAGN* **2011,** *24*, 721-726.

14. Ortmann, F.; Bechstedt, F.; Hannewald, K., Theory of charge transport in organic crystals: Beyond Holstein's small-polaron model. *Physical Review B* **2009,** *79* (23), 235206.

15. Hulea, I. N.; Fratini, S.; Xie, H.; Mulder, C. L.; Iossad, N. N.; Rastelli, G.; Ciuchi, S.; Morpurgo, A. F., Tunable Frohlich polarons in organic single-crystal transistors. *Nature materials* **2006,** *5* (12), 982-986.

16. Cheng, J.; VandeVondele, J.; Sprik, M., Identifying Trapped Electronic Holes at the Aqueous TiO2 Interface. *J. Phys. Chem. C* **2014,** *118* (10), 5437-5444.

17. Li, B.; Zhao, J.; Onda, K.; Jordan, K. D.; Yang, J. L.; Petek, H., Ultrafast interfacial proton-coupled electron transfer. *Science* **2006,** *311* (5766), 1436-1440.

18. Man, I. C.; Su, H.-Y.; Calle-Vallejo, F.; Hansen, H. A.; Martínez, J. I.; Inoglu, N. G.; Kitchin, J.; Jaramillo, T. F.; Nørskov, J. K.; Rossmeisl, J., Universality in Oxygen Evolution Electrocatalysis on Oxide Surfaces. *ChemCatChem* **2011,** *3* (7), 1159-1165.

19. Chen, X.; Choing, S. N.; Aschaffenburg, D. J.; Pemmaraju, C. D.; Prendergast, D.; Cuk, T., The formation time of Ti-O• and Ti-O•-Ti radicals at the n-SrTiO3/aqueous interface during photocatalytic water oxidation. *Journal of the American Chemical Society* **2017,** *139*, 1830-1841.

20. Divanis, S.; Kutlusoy, T.; Ingmer Boye, I. M.; Man, I. C.; Rossmeisl, J., Oxygen evolution reaction: a perspective on a decade of atomic scale simulations. *Chemical Science* **2020,** *11* (11), 2943-2950.

21. Deskins, N. A.; Dupuis, M., Intrinsic Hole Migration Rates in TiO2 from Density Functional Theory. *The Journal of Physical Chemistry C* **2009,** *113* (1), 346-358.

22. Garrett, B. C.; Dixon, D. A.; Camaioni, D. M.; Chipman, D. M.; Johnson, M. A.; Jonah, C. D.; Kimmel, G. A.; Miller, J. H.; Rescigno, T. N.; Rossky, P. J.; Xantheas, S. S.; Colson, S. D.; Laufer, A. H.; Ray, D.; Barbara, P. F.; Bartels, D. M.; Becker, K. H.; Bowen, H.; Bradforth, S. E.; Carmichael, I.; Coe, J. V.; Corrales, L. R.; Cowin, J. P.; Dupuis, M.; Eisenthal, K. B.; Franz, J. A.; Gutowski, M. S.; Jordan, K. D.; Kay, B. D.; LaVerne, J. A.; Lymar, S. V.; Madey, T. E.; McCurdy, C. W.; Meisel, D.; Mukamel, S.; Nilsson, A. R.; Orlando, T. M.; Petrik, N. G.; Pimblott, S. M.; Rustad, J. R.; Schenter, G. K.; Singer, S. J.; Tokmakoff, A.; Wang, L. S.; Wittig, C.; Zwier, T. S., Role of water in electron-initiated processes and radical chemistry: Issues and scientific advances. *Chemical Reviews* **2005,** *105* (1), 355-389.

23. Chen, J.; Li, Y. F.; Sit, P.; Selloni, A., Chemical Dynamics of the First Proton-Coupled Electron Transfer of Water Oxidation on TiO2 Anatase. *Journal of the American Chemical Society* **2013,** *135* (50), 18774-18777.

24. Di Valentin, C.; Selloni, A., Bulk and Surface Polarons in Photoexcited Anatase TiO2. *The Journal of Physical Chemistry Letters* **2011,** *2* (17), 2223-2228.

25. Herlihy, D. M.; Waegele, M. M.; Chen, X.; Pemmaraju, C. D.; Prendergast, D.; Cuk, T., Detecting the oxyl radical of photocatalytic water oxidation at an n-SrTiO3/aqueous interface through its subsurface vibration. *Nat Chem* **2016,** *8* (6), 549-55.

26. Chen, X.; Aschaffenburg, D.; Cuk, T., One-electron intermediates of water oxidation & the role of solvation in their stability. *J. Mater. Chem. A* **2017,** *5* (23), 11410-11417.

27. Zandi, O.; Hamann, T. W., Determination of photoelectrochemical water oxidation intermediates on haematite electrode surfaces using operando infrared spectroscopy. *Nat Chem* **2016,** *8* (8), 778-83.

28. Klahr, B.; Gimenez, S.; Fabregat-Santiago, F.; Bisquert, J.; Hamann, T. W., Photoelectrochemical and Impedance Spectroscopic Investigation of Water Oxidation with "Co-Pi"-Coated Hematite Electrodes. *Journal of the American Chemical Society* **2012,** *134* (40), 16693-16700.

29. Klahr, B.; Hamann, T., Water Oxidation on Hematite Photoelectrodes: Insight into the Nature of Surface States through In

Situ Spectroelectrochemistry. *The Journal of Physical Chemistry C* **2014,** *118* (19), 10393-10399.

30. Liu, H.; Frei, H., Observation of O–O Bond Forming Step of Molecular Co4O4 Cubane Catalyst for Water Oxidation by Rapid-Scan FT-IR Spectroscopy. *ACS Catalysis* **2020,** *10* (3), 2138-2147.

31. Zhang, M.; de Respinis, M.; Frei, H., Time-resolved observations of water oxidation intermediates on a cobalt oxide nanoparticle catalyst. *Nat Chem* **2014,** *6* (4), 362-7.

32. Zhang, M.; Frei, H., Towards a Molecular Level Understanding of the Multi-Electron Catalysis of Water Oxidation on Metal Oxide Surfaces. *Catalysis Letters* **2014,** *145* (1), 420-435.

33. Frei, H., Water oxidation investigated by rapid-scan FT-IR spectroscopy. *Current Opinion in Chemical Engineering* **2016,** *12*, 91-97.

34. Zhang, M.; Frei, H., Water Oxidation Mechanisms of Metal Oxide Catalysts by Vibrational Spectroscopy of Transient Intermediates. In *Annual Review of Physical Chemistry, Vol 68*, Johnson, M. A.; Martinez, T. J., Eds. 2017; Vol. 68, pp 209-231.

35. Hunter, B. M.; Thompson, N. B.; Müller, A. M.; Rossman, G. R.; Hill, M. G.; Winkler, J. R.; Gray, H. B., Trapping an Iron(VI) Water-Splitting Intermediate in Nonaqueous Media. *Joule* **2018,** *2* (4), 747-763.

36. Zhang, B.; Daniel, Q.; Fan, L.; Liu, T.; Meng, Q.; Sun, L., Identifying Mn(VII)-oxo Species during Electrochemical Water Oxidation by Manganese Oxide. *iScience* **2018,** *4*, 144-152.

37. Diaz-Morales, O.; Ferrus-Suspedra, D.; Koper, M. T. M., The importance of nickel oxyhydroxide deprotonation on its activity towards electrochemical water oxidation. *Chem Sci* **2016,** *7* (4), 2639-2645.

38. Chen, X.; Aschaffenburg, D. J.; Cuk, T., Selecting between two transition states by which water oxidation intermediates decay on an oxide surface. *Nature Catalysis* **2019,** *2* (9), 820-827.

39. Bullock, R. M.; Chen, J. G.; Gagliardi, L.; Chirik, P. J.; Farha, O. K.; Hendon, C. H.; Jones, C. W.; Keith, J. A.; Klosin, J.; Minteer, S. D.; Morris, R. H.; Radosevich, A. T.; Rauchfuss, T. B.; Strotman, N. A.; Vojvodic, A.; Ward, T. R.; Yang, J. Y.; Surendranath, Y., Using nature's blueprint to expand catalysis with Earth-abundant metals. *Science* **2020,** *369* (6505), eabc3183.

40. Bandaranayake, S.; Hruska, E.; Londo, S.; Biswas, S.; Baker, L. R., Small Polarons and Surface Defects in Metal Oxide Photocatalysts Studied Using XUV Reflection–Absorption Spectroscopy. *The Journal of Physical Chemistry C* **2020,** *124* (42), 22853-22870.

41. Nong, H. N.; Falling, L. J.; Bergmann, A.; Klingenhof, M.; Tran, H. P.; Spöri, C.; Mom, R.; Timoshenko, J.; Zichittella, G.; Knop-Gericke, A.; Piccinin, S.; Pérez-Ramírez, J.; Cuenya, B. R.; Schlögl, R.; Strasser, P.; Teschner, D.; Jones, T. E., Key role of chemistry versus bias in electrocatalytic oxygen evolution. *Nature* **2020,** *587* (7834), 408-413.

42. Boettcher, S. W.; Surendranath, Y., Heterogeneous electrocatalysis goes chemical. *Nature Catalysis* **2021,** *4* (1), 4-5.

43. Ketteler, G.; Yamamoto, S.; Bluhm, H.; Andersson, K.; Starr, D. E.; Ogletree, D. F.; Ogasawara, H.; Nilsson, A.; Salmeron, M., The nature of water nucleation sites on TiO2(110) surfaces revealed by ambient pressure X-ray photoelectron spectroscopy. *J. Phys. Chem. C* **2007,** *111* (23), 8278-8282.

44. Newberg, J. T.; Starr, D. E.; Yamamoto, S.; Kaya, S.; Kendelewicz, T.; Mysak, E. R.; Porsgaard, S.; Salmeron, M. B.; Brown, G. E.; Nisson, A.; Bluhm, H., Autocatalytic Surface Hydroxylation of MgO(100) Terrace Sites Observed under Ambient Conditions. *J. Phys. Chem. C* **2011,** *115* (26), 12864-12872.

45. Newberg, J. T.; Starr, D. E.; Yamamoto, S.; Kaya, S.; Kendelewicz, T.; Mysak, E. R.; Porsgaard, S.; Salmeron, M. B.; Brown, G. E.; Nilsson,

A.; Bluhm, H., Formation of hydroxyl and water layers on MgO films studied with ambient pressure XPS. *Surf. Sci.* **2011,** *605* (1-2), 89-94.

46. Hinojosa, B. B.; Van Cleve, T.; Asthagiri, A., A first-principles study of H2O adsorption and dissociation on the SrTiO3(100) surface. *Mol. Simul.* **2010,** *36* (7-8), 604-617.

47. Aschaffenburg, D. J.; Kawasaki, S.; Pemmaraju, C. D.; Cuk, T., Accuracy in Resolving the First Hydration Layer on a Transition-Metal Oxide Surface: Experiment (AP-XPS) and Theory. *The Journal of Physical Chemistry C* **2020,** *124* (39), 21407-21417.

48. Cheng, J.; Sprik, M., Acidity of the Aqueous Rutile TiO2(110) Surface from Density Functional Theory Based Molecular Dynamics. *Journal of Chemical Theory and Computation* **2010,** *6* (3), 880-889.

49. Yamaguchi, A.; Inuzuka, R.; Takashima, T.; Hayashi, T.; Hashimoto, K.; Nakamura, R., Regulating proton-coupled electron transfer for efficient water splitting by manganese oxides at neutral pH. *Nature Communications* **2014,** *5* (1), 4256.

50. Eigen, M., Proton Transfer, Acid-Base Catalysis, and Enzymatic Hydrolysis. Part I: ELEMENTARY PROCESSES. *Angewandte Chemie International Edition in English* **1964,** *3* (1), 1-19.

51. Janotti, A.; Varley, J. B.; Choi, M.; Van de Walle, C. G., Vacancies and small polarons in SrTiO₃. *Phys. Rev. B* **2014,** *90* (8), 085202.

52. Marcus, R. A., ON THE THEORY OF OXIDATION-REDUCTION REACTIONS INVOLVING ELECTRON TRANSFER .1. *J. Chem. Phys.* **1956,** *24* (5), 966-978.

53. Truhlar, D. G.; Garrett, B. C.; Klippenstein, S. J., Current Status of Transition-State Theory. *J. Phys. Chem.* **1996,** *100*, 12771-12800.

54. Hong, W. T.; Risch, M.; Stoerzinger, K. A.; Grimaud, A.; Suntivich, J.; Shao-Horn, Y., Toward the rational design of non-precious transition metal oxides for oxygen electrocatalysis. *Energy Environ. Sci.* **2015,** *8* (5), 1404-1427.

55. Suntivich, J.; May, K. J.; Gasteiger, H. A.; Goodenough, J. B.; Shao-Horn, Y., A perovskite oxide optimized for oxygen evolution catalysis from molecular orbital principles. *Science* **2011,** *334* (6061), 1383-5.

56. Hansen, H. A.; Rossmeisl, J.; Norskov, J. K., Surface Pourbaix diagrams and oxygen reduction activity of Pt, Ag and Ni(111) surfaces studied by DFT. *Physical Chemistry Chemical Physics* **2008,** *10*, 3607.

57. Eichhorn, J.; Reyes-Lillo, S. E.; Roychoudhury, S.; Sallis, S.; Weis, J.; Larson, D. M.; Cooper, J. K.; Sharp, I. D.; Prendergast, D.; Toma, F. M., Revealing Nanoscale Chemical Heterogeneities in Polycrystalline Mo-BiVO4 Thin Films. *Small* **2020,** *16* (35), 2001600.

58. Strickler, A. L.; Higgins, D.; Jaramillo, T. F., Crystalline Strontium Iridate Particle Catalysts for Enhanced Oxygen Evolution in Acid. *ACS Applied Energy Materials* **2019,** *2* (8), 5490-5498.

59. Xu, Y.; Schoonen, M. A. A., The absolute energy positions of conduction and valence bands of selected semiconducting minerals. *American Mineralogist* **2000,** *85* (3-4), 543-556.

60. Aschaffenburg, D. J.; Chen, X.; Cuk, T., Faradaic oxygen evolution from SrTiO3 under nano- and femto-second pulsed light excitation. *Chem Commun (Camb)* **2017,** *53* (53), 7254-7257.

61. Waegele, M. M.; Chen, X.; Herlihy, D. M.; Cuk, T., How Surface Potential Determines the Kinetics of the First Hole Transfer of Photocatalytic Water Oxidation. *Journal of the American Chemical Society* **2014,** *136* (30), 10632-10639.

62. Mesa, C. A.; Francas, L.; Yang, K. R.; Garrido-Barros, P.; Pastor, E.; Ma, Y.; Kafizas, A.; Rosser, T. E.; Mayer, M. T.; Reisner, E.; Gratzel, M.; Batista, V. S.; Durrant, J. R., Multihole water oxidation catalysis on haematite photoanodes revealed by operando spectroelectrochemistry and DFT. *Nat Chem* **2020,** *12* (1), 82-89.

63. Le Formal, F.; Pastor, E.; Tilley, S. D.; Mesa, C. A.; Pendlebury, S. R.; Gratzel, M.; Durrant, J. R., Rate law analysis of water oxidation on a hematite surface. *J Am Chem Soc* **2015,** *137* (20), 6629-37.

64. Kafizas, A.; Ma, Y.; Pastor, E.; Pendlebury, S. R.; Mesa, C.; Francàs, L.; Le Formal, F.; Noor, N.; Ling, M.; Sotelo-Vazquez, C.; Carmalt, C. J.; Parkin, I. P.; Durrant, J. R., Water Oxidation Kinetics of Accumulated Holes on the Surface of a TiO2 Photoanode: A Rate Law Analysis. *ACS Catalysis* **2017,** *7* (7), 4896-4903.

65. Ma, Y.; Mesa, C. A.; Pastor, E.; Kafizas, A.; Francàs, L.; Le Formal, F.; Pendlebury, S. R.; Durrant, J. R., Rate Law Analysis of Water Oxidation and Hole Scavenging on a BiVO4 Photoanode. *ACS Energy Letters* **2016,** *1* (3), 618-623.

66. I. Vinogradov; S. Singh; H. Lyle; A. Mandal*; J. Rossmeisl; Cuk*, T., Measuring theoretical descriptors of water oxidation: Free energy differences between intermediates by time-resolved optical spectroscopy. *Nature Materials, Under-revision* **2020,** (Preprint at ChemRxiv).

67. Farrow, C. L.; Bediako, D. K.; Surendranath, Y.; Nocera, D. G.; Billinge, S. J. L., Intermediate-Range Structure of Self-Assembled Cobalt-Based Oxygen-Evolving Catalyst. *Journal of the American Chemical Society* **2013,** *135* (17), 6403-6406.

68. Hadt, R. G.; Hayes, D.; Brodsky, C. N.; Ullman, A. M.; Casa, D. M.; Upton, M. H.; Nocera, D. G.; Chen, L. X., X-ray Spectroscopic Characterization of Co(IV) and Metal-Metal Interactions in Co4O4: Electronic Structure Contributions to the Formation of High-Valent States Relevant to the Oxygen Evolution Reaction. *J Am Chem Soc* **2016,** *138* (34), 11017-30.

69. Brodsky, C. N.; Hadt, R. G.; Hayes, D.; Reinhart, B. J.; Li, N.; Chen, L. X.; Nocera, D. G., In situ characterization of cofacial Co(IV) centers in Co₄O₄ cubane: Modeling the high-valent active site in oxygen-evolving catalysts. *Proceedings of the National Academy of Sciences* **2017,** *114* (15), 3855-3860.

70. Forster, M.; Cheung, D. W. F.; Gardner, A. M.; Cowan, A. J., Potential and pitfalls: On the use of transient absorption spectroscopy for in situ and operando studies of photoelectrodes. *The Journal of Chemical Physics* **2020,** *153* (15), 150901.

71. Pendlebury, S. R.; Wang, X.; Le Formal, F.; Cornuz, M.; Kafizas, A.; Tilley, S. D.; Grätzel, M.; Durrant, J. R., Ultrafast Charge Carrier Recombination and Trapping in Hematite Photoanodes under Applied Bias. *Journal of the American Chemical Society* **2014,** *136* (28), 9854-9857.

72. Pham, H. H.; Cheng, M.-J.; Frei, H.; Wang, L.-W., Surface Proton Hopping and Fast-Kinetics Pathway of Water Oxidation on Co3O4(001) Surface. *ACS Catalysis* **2016,** *6* (8), 5610-5617.

73. Sivasankar, N.; Weare, W. W.; Frei, H., Direct Observation of a Hydroperoxide Surface Intermediate upon Visible Light-Driven Water Oxidation at an Ir Oxide Nanocluster Catalyst by Rapid-Scan FT-IR Spectroscopy. *Journal of the American Chemical Society* **2011,** *133* (33), 12976-12979.

74. Zhang, Y.; Zhang, H.; Liu, A.; Chen, C.; Song, W.; Zhao, J., Rate-Limiting O–O Bond Formation Pathways for Water Oxidation on Hematite Photoanode. *Journal of the American Chemical Society* **2018,** *140* (9), 3264-3269.